Active and Passive Remote Sensing of Precipitation

Haonan Chen[a], **Rob Cifelli**[b], **and Pingping Xie**[c], [a] Colorado State University, Fort Collins, CO, United States; [b] National Oceanic and Atmospheric Administration, Boulder, CO, United States; and [c] National Oceanic and Atmospheric Administration, College Park, MD, United States

This is an update of R.R. Ferraro, G. Skofronick-Jackson, Y. Hong, K. Zhang, 4.02 - Precipitation, Editor(s): Shunlin Liang, Comprehensive Remote Sensing, Elsevier, 2018, Pages 4–24, ISBN 9780128032213, https://doi.org/10.1016/B978-0-12-409548-9.10385-9.

Key Points

- Fundamentals of active and passive remote sensing of precipitation are briefly reviewed.
- The strengths and weaknesses of precipitation retrieval techniques using measurements from different remote sensing platforms are summarized.
- Example applications of active radar and passive satellite precipitation datasets are provided for monitoring and predicting water-related hazards.

https://doi.org/10.1016/B978-0-443-13220-9.00034-2

Abstract

Precipitation is a vital component in the global, continental, and regional hydrologic cycles. Accurate precipitation observations and estimates are critical for providing improved situational awareness of hazards associated with both too much (e.g., floods and debris flows) and too little water (e.g., drought and wildfire). Advanced quantitative precipitation information is also important in addressing various weather, water, and energy challenges to improve climate adaptation and resilience. Compared to rain gauges, remote sensing instruments such as radars and satellites have great advantages in monitoring precipitation and its evolution at various spatiotemporal scales. This article presents a brief description of fundamentals of active and passive remote sensing of precipitation. The strengths and weaknesses of various remote sensing platforms, as well as precipitation retrieval techniques for ground-based and spaceborne radars, visible, infrared, and passive microwave measurements from low Earth orbiting (LEO) and geostationary orbiting (GEO) satellites, are summarized. Example applications of remote sensing precipitation datasets are also provided to highlight the use of radars and satellites for monitoring and predicting water-related hazards.

Introduction

Precipitation plays a key role in understanding the global, continental, and regional water cycles and observations are critical for providing improved situational awareness of hazards associated with both too much (e.g., floods and debris flows) and too little water (e.g., drought and wildfire). Accurate precipitation measurements or estimates are also vital in addressing various weather, water, climate, and energy challenges in the context of climate change. For example, the National Oceanic and Atmospheric Administration (NOAA) is currently leading the effort to update Precipitation Frequency and Probable Maximum Precipitation estimates with climate change information. These products are used extensively by federal, state, and local water agencies, transportation planners, and other stakeholders to inform infrastructure design and to improve climate adaptation and resilience.

While pointwise rain gauges are conventionally used for precipitation estimation, they are typically restricted to populated areas over land. It is difficult to capture precipitation features such as spatial distribution using rain gauge data and rain gauge networks must be rigorously maintained to ensure the accuracy of the measurements. Compared to rain gauges, remote sensing instruments, including radars and satellites, have demonstrated great advantages in monitoring precipitation and its evolution at various scales. In particular, ground-based weather radars can provide spatially continuous observations over a large area with small temporal sampling intervals (e.g., Bringi and Chandrasekar, 2001; Chen and Chandrasekar, 2015a; Cifelli et al., 2024). Therefore, ground-based weather radar network is the primary system for quantitative precipitation estimation (QPE) in many nations. On the other hand, satellites can fill in the huge data voids of rain gauge and ground-based weather radar networks, especially over mountains and oceans where rain gauges or radars are sparsely deployed or completely absent (Kidd et al., 2017, 2021). With satellites and radars operating for several decades, both regional and global precipitation climatology information has been developed, although many challenges still remain in understanding the physical processes that drive precipitation patterns as well as the accuracy of the observations.

A number of different instruments and retrieval techniques are used to estimate precipitation from radars and satellites. The strengths and weaknesses of various remote sensing methods are briefly summarized in **Table 1**, whereas details on the general classes of methods are provided in the following sections. Radars that are used to estimate precipitation are generally categorized into single-polarization and dual-polarization systems, whereas satellites are typically categorized into low Earth orbiting (LEO) and geostationary orbiting (GEO) satellites. Then, the various retrieval algorithms can be classified based on their observing

Table 1 Summary of precipitation remote sensing techniques and their attributes.

Observation spectrum	*Platforms*	*Sensor Examples*	*Strength*	*Weakness*
Active microwave (AMW)	Ground-based radars	NEXRAD CSU-CHILL radar NASA NPOL radar	Direct measure of precipitation High spatiotemporal resolution	Poor coverage over mountains and oceans
AMW	LEO satellites	CloudSat CPR GPM DPR Fengyun-3G DPR	Direct measure of vertical structure of rain	Narrow swath width Precipitation rate sensitivity
Visible (VIS)	GEO satellites LEO satellites	GOES Imager VIIRS	Cloud type Cloud evolution	Cloud tops Indirect rain rate
Infrared (IR)	GEO satellites LEO satellites	GOES Imager VIIRS	Cloud temperature cloud evolution	Cirrus contamination Indirect rain rate
Passive microwave (PMW)	LEO satellites	SSM/I; GMI; AMSR-2; ATMS	Direct measure of rain, especially over ocean	Temporal sampling Indirect precipitation rate (land)

spectrum (e.g., active microwave-AMW, visible-VIS, infrared-IR, passive microwave-PMW). In addition, there are techniques that rely on a combination of these spectrums, commonly referred to as multispectral approaches. More recently, a number of methods combine the best attributes of each individual product, and in some cases, in situ data; these are referred to as blended algorithms. The goal of this chapter is to describe this wide spectrum of precipitation remote sensing methods, highlight their strengths and weaknesses, and provide examples of their applications.

Active Microwave Methods

Ground-Based Radars

Ground-based radar has been used for precipitation estimation since its earliest application in meteorology. In contrast to passive microwave radiometers, radars, as active microwave sensors, provide their own source of microwave radiation. Traditionally, precipitation estimation with radar has been accomplished through the radar reflectivity Z and rainfall rate R relationships, also known as $Z-R$ relations. However, it has been found that $Z-R$ relations depend greatly on local raindrop size distributions (DSD), which may vary across different rainfall regimes, even within a single precipitation system. It is often a nontrivial task to find an ideal $Z-R$ relation to represent the microphysical properties of all the storms. Since the introduction of polarization diversity in meteorological radar (Seliga and Bringi, 1976), a large amount of effort has been devoted to polarimetric radar systems and their weather applications. Through the dual-polarization radar measurements, including reflectivity, differential reflectivity (Z_{dr}), specific differential propagation phase (K_{dp}), and co-polar correlation coefficient (ρ_{hv}), radar data quality can be considerably enhanced. In addition, different hydrometeor types can be identified, and DSD information can be gleaned in more effective ways with the dual-polarization observations (Bringi and Chandrasekar, 2001). Currently, all the radar stations comprising the US National Weather Service (NWS) Weather Surveillance Radar-1988 Doppler (WSR-88D) network, or the Next-Generation Radar (NEXRAD) network, are operating in dual-polarization mode. One of the main considerations for the dual-polarization upgrade was better QPE.

A number of dual-polarization radar rainfall estimation algorithms have been developed in previous studies, using Z, Z_{dr}, K_{dp} or a combination of these observables. Although there is no standard criterion to determine which estimator to employ for a given set of dual-polarization measurements, the hydrometeor classification-based methods are widely used in the weather radar community. Popular examples include the operational WSR-88D algorithm described in Giangrande and Ryzhkov (2008) and the dual-polarization radar operational processing system (DROPS) developed at Colorado State University (Cifelli et al., 2011; Chen et al., 2017). As shown in **Fig. 1**, such a QPE system typically consists of three components, namely, data quality control, classification of different hydrometeor types, and precipitation quantification with appropriate polarimetric radar rainfall relations.

In order to obtain the specific radar rainfall relations, local DSD measurements are often required, which can be used to simulate the dual-polarization radar observables at different frequencies using a scattering model such as the T-matrix method (Waterman, 1965). Based on the simulated radar observations and corresponding rainfall rates computed directly from the DSD data, nonlinear

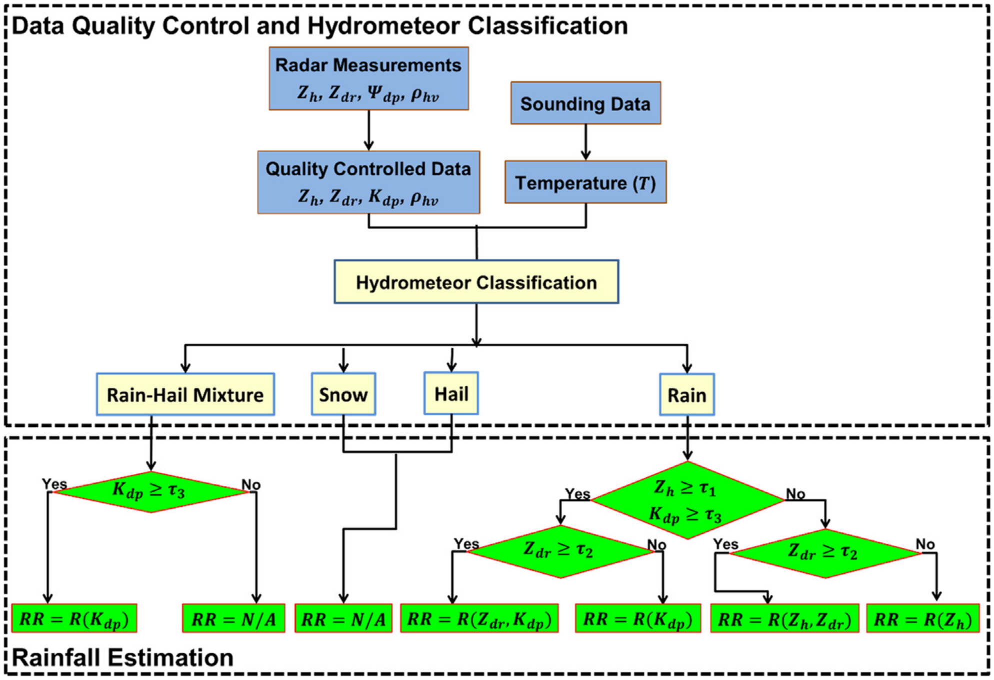

Fig. 1 A polarimetric weather radar rainfall estimation algorithm driven by hydrometeor classification results.

regression can be applied to derive the specific relations including $R(Z_h)$, $R(Z_h, Z_{dr})$, $R(K_{dp})$ and $R(Z_{dr}, K_{dp})$. **Fig. 2** illustrates example polarimetric observations from the S-band KFWS WSR-88D radar during a storm event at 12:31UTC, June 09, 2013, as well as the corresponding rainfall rate estimated using the DROPS method.

Combining the polarimetric observations and precipitation estimates from ~160 WSR-88D radars, as well as rain gauges and other auxiliary environmental information, the National Oceanic and Atmospheric Administration (NOAA) has developed a multi-radar multi-sensor (MRMS) system to produce precipitation estimates (Zhang et al., 2016a). The MRMS system has been operational since 2015 and the MRMS products are widely used for various hydrometeorological applications. **Fig. 3** shows an example gauge-corrected radar hourly precipitation product from the MRMS system during a fast-moving severe thunderstorm on December 11, 2021. This event developed as a trough progressed eastward across the U. S. and produced the devastating tornado outbreak of 10–11 December 2021 across the Southern U S and Ohio Valley.

Nevertheless, one limitation of the operational, long-range microwave (e.g., S- or C-band) radars is the inability to cover the lower part of atmosphere due to the Earth's curvature and terrain blockage. To address these issues and enhance resolution of operational weather radar network, the US National Science Foundation Engineering Research Center (NSF-ERC) for Collaborative Adaptive Sensing of the Atmosphere (CASA) introduced an innovative collaborative and dynamic sensing paradigm, which utilizes a dense network of small, low-power, X-band dual-polarization radars to improve QPE and hazardous weather monitoring and prediction (McLaughlin et al., 2009). The high-resolution observations and post-event case studies from CASA's first research testbed in Southwestern Oklahoma demonstrated the great potential of this new sensing paradigm. The great success of CASA research radar network has also led to urban scale implementations of this concept across the world, such as the research-to-operation testbed in the Dallas-Fort Worth (DFW) metroplex (Chen and Chandrasekar, 2015a, 2018; Chandrasekar et al., 2018), the operational gap-filing radar network in the San Francisco Bay Area (Cifelli et al., 2018, 2024), and the operational phased-array weather radar network in Southern China (Zhao et al., 2024). At X-band or higher frequency, the choice of precipitation estimation algorithm is influenced by attenuation since Z_h and Z_{dr} must be corrected for attenuation before using them for quantitative applications. As such, K_{dp} is often solely used for QPE as the differential phase is not affected by attenuation and is not sensitive to partial beam blockage or radar system calibration error (Bringi and Chandrasekar, 2001; Chen and Chandrasekar, 2015b).

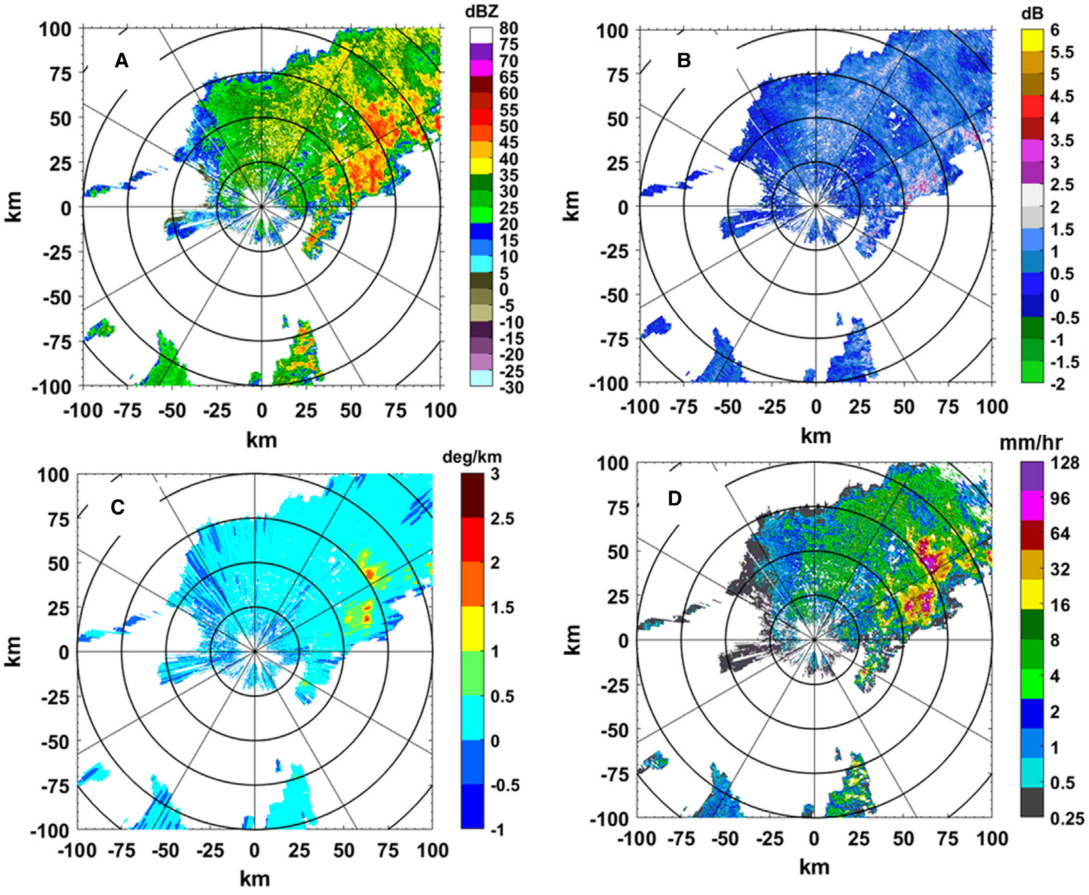

Fig. 2 Polarimetric observations from the S-band KFWS WSR-88D radar at 12:31UTC, June 09, 2013: (A) reflectivity Z_h, (B) differential reflectivity Z_{dr}, and (C) specific differential phase K_{dp}. (D) shows the corresponding rainfall rate (R) estimates using the method illustrated in **Fig. 1**.

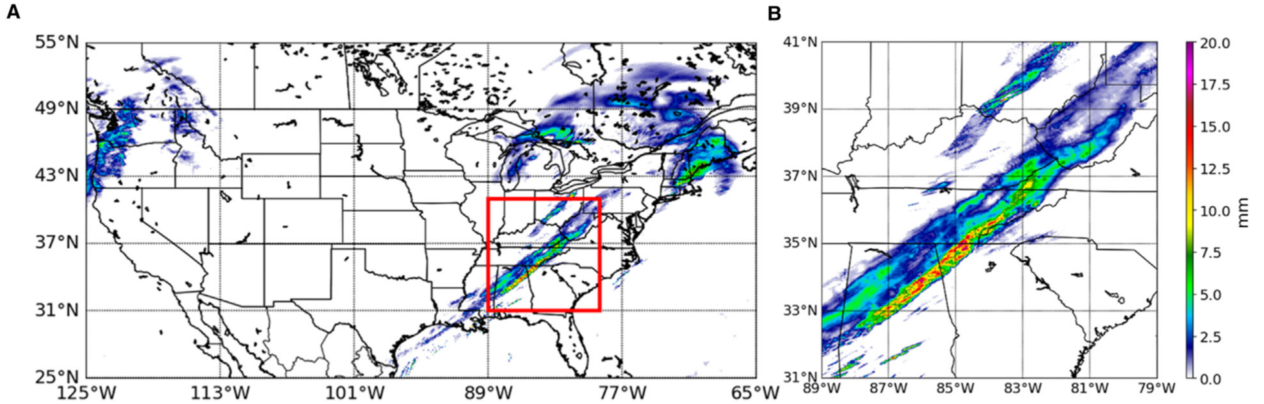

Fig. 3 (A) Gauge-corrected radar hourly precipitation estimates from the NOAA MRMS system for the hour ending at 17:00UTC, December 11, 2021. The line of enhanced rainfall draped across the southeast US (highlighted in the red box) is associated with a widespread tornado outbreak in this region. (B) Zoomed-in version of the precipitation field in the red box in (A).

Another potential way to improve conventional radar QPE is using artificial intelligence and machine learning techniques. Compared to traditional parametric radar rainfall relations, machine learning can often better extract precipitation information from the multidimensional multiparameter polarimetric radar observations (Chen et al., 2019). Although a detailed explanation of machine learning-based radar QPE methods is beyond the scope of this article, interested readers are referred to Li et al. (2023, 2024a,b) for demonstration studies based on WSR-88D observations. These studies suggest that machine learning can capture more spatial correlation of precipitation from dual-polarization radar data and effectively map the connection between radar observations aloft and surface rainfall rates.

Space-Based Radars

One way to avoid the coverage limitations of ground-based radar sampling is to deploy radars on spaced-based platforms. Due to deployment challenges and tradeoff between resolution and antenna size, only radars at frequencies greater than 10 GHz are practical for space-based platforms (Fujita and Satake, 1997). At these frequencies, the two-way path integrated attenuation (PIA) becomes significant over the rain depth of kilometers, especially during moderate to heavy rain events. Unless reflectivity is corrected for attenuation effects, the reflectivity-based rain rate estimate will have a bias, which increases with frequency as a result of an increase in PIA.

Techniques have been developed to remove the effects of attenuation for space-based radar applications. The study by Hitschfeld and Bordan (1954) was one of the first to propose a method for directly correcting measured reflectivity for attenuation. After attenuation correction, rain rates are estimated using the corrected reflectivity through $Z-R$ relations. The Hitschfeld-Bordan (HB) solution gives reasonable estimates if the attenuation is small and the radar is well-calibrated. When these conditions are not met, this method can become unstable. Numerous retrieval methods have been developed that incorporate this early work along with the more recent technique of constraining the retrievals using PIA derived from surface reference technique (SRT) (Iguchi and Meneghini, 1994; Meneghini et al., 2004, 2015). SRT relies on a reference measurement of the radar return from the surface in rain-free conditions. For example, if the surface returns for a particular incidence angle and surface types are stable, the difference in surface returns for rain-filled and rain-free radar beams can be ascribed to the effects of attenuation by precipitation. The SRT method provides a reasonable way to monitor PIA over the ocean. Over land, particularly at near-nadir incidence where the surface scattering cross section is usually highly variable in both space and time, the method is less reliable (Meneghini et al., 2004).

In addition, although these methods work fairly well for Ku-band Tropical Rainfall Measurement Mission (TRMM) Precipitation Radar (PR) and Ku/Ka band Global Precipitation Measurement (GPM) Dual-frequency Precipitation Radar (DPR), it is challenging to use these approaches when attenuation is strong such as the W-band cloud profiling radar (CPR) aboard CloudSat. Another example of rainfall retrieval technique from spaceborne radar is to use the attenuation directly caused by rainfall (Matrosov, 2007). This method takes advantage of high attenuation in rain and low variability of nonattenuated reflectivity and uses estimates of height derivatives of attenuated reflectivity. These estimates are then related to rain rates. Early results based on the CloudSat CPR measurements demonstrates a possibility of rain rate profile retrieval (Matrosov, 2007; Mitrescu et al., 2010).

Here, a brief review of several space-based precipitation radars is provided, including TRMM PR, CloudSat CPR, GPM DPR, and the Ka-band radar for the RainCube mission.

TRMM-PR

In operation for nearly 18 years (1997–2014), the TRMM PR was the first active passive microwave instrument designed to measure rain from space (Kummerow et al., 1998). TRMM was a LEO satellite orbiting at 402.5 km above the Earth surface. Its subtrack covered latitudes of ± 35°. TRMM PR was a cross-track Ku-band (13 GHz) radar that surveyed a swath of 220 km at a horizontal resolution of 4.3 km, and a vertical distribution with the height resolution of 250 m. PR provided for the first time a direct, fine-scale, view of both the vertical and horizontal distribution of precipitation across the global tropics. This information has advanced our fundamental understanding of precipitation processes, as well as providing validation for model simulations and forecasts.

Several iterations of the PR rain retrieval algorithm have occurred since its original operation. Initially, the PR rain retrieval algorithm used a hybrid of the HB and SRT methods to correct for attenuation (Iguchi et al., 2000). When the SRT is reliable, the radar-rain rate relations are adjusted so that the HB path-attenuated estimate is equal to that of SRT. When the SRT is unreliable, the HB method is usually used along with radar-rainfall relation derived from ground-based disdrometer measurements, conditioned on rain type, to provide vertical profiles of rain rate.

There are some limitations to the TRMM PR-its sensitivity is about 18 dBZ and thus cannot retrieve very light rainfall rates below $\sim$0.5 mm h^{-1}. Additionally, there are adjustments that need to be accounted for over mountainous and rough terrain. Several improvements to the original algorithms have been made over the years (e.g., Takahashi and Iguchi, 2008; Iguchi et al., 2009).

CloudSat

Launched in April 2006 and decommissioned in December 2023, CloudSat was the first millimeter wavelength (W-band, 94 GHz) cloud profiling radar in space (Stephens et al., 2002). It was flown in the A-Train configuration and used synergistically with other satellites and sensors to gain a better understanding of cloud-aerosol-precipitation processes (Fan et al., 2016). The CloudSat CPR was a near nadir-pointing downward looking radar with 500 m vertical resolution, 1.7 km horizontal resolution, and sensitivity of -30 dBZ. The design concept of CPR was to provide vertical cross section of nonprecipitating cloud liquid and ice water content and particle size. At the altitude of 750 km, the CPR provided vertical profiles of radar reflectivity. Although the main objective of CPR was to provide global information on clouds, it also resolved many precipitation systems, in particular, light rain and snow that were often missed by the TRMM PR (L'Ecuyer and Stephens, 2002; Haynes and Stephens, 2007; Matrosov, 2007; Liu, 2008). As such, it has been useful for gaining a better understanding of high-latitude precipitation features (Hong and Liu, 2015) and tropical cloud and precipitation systems, including tropical cyclones (Tourville et al., 2015), although CloudSat CPR would attenuate at higher rain rates and precipitation rates above $\sim$5 mm h^{-1} cannot be estimated reliably (Mitrescu et al., 2010).

The European Space Agency (ESA), in cooperation with the Japan Aerospace Exploration Agency (JAXA), has implemented the Earth Cloud, Aerosol and Radiation Explorer (EarthCARE) satellite mission to measure global profiles of aerosols, clouds and precipitation properties together with radiative fluxes and derived heating rates (Wehr et al., 2023). The EarthCARE mission was launched on May 28, 2024 and is flying a cloud radar similar to CPR on CloudSat, but with greater sensitivity and higher spatial resolution.

GPM DPR

GPM is a joint US - Japan mission designed to extend TRMM's observations of precipitation to higher latitudes, with more frequent sampling (Hou et al., 2014; Skofronick-Jackson et al., 2017). The GPM Core Observatory satellite was launched in February 2014 and carries a dual-frequency, cross-track scanning, Ku/Ka-band (13.6/35.5 GHz) precipitation radar, i.e., the DPR (Iguchi et al., 2002). The addition of the Ka-band radar brings the sensitivity down to 12 dBZ, thus the advantages of the DPR over the single-frequency TRMM PR include: enhanced sensitivity at light rain rates (down to 0.2 mm h^{-1}); information on the particle size distribution in rain and snow; and improvements in the identification of vertical layers consisting of mixed phase, frozen and liquid particles (Toyoshima et al., 2015). Particle size estimation follows from Mie scattering effects in that the difference in radar reflectivity at the two frequencies (also known as dual-frequency ratio) provides an estimate of the mean particle size of the distribution (Meneghini et al., 1989, 1992; Meneghini and Kozu, 1990; Kuo et al., 2004). This dual-frequency measurement allows for recovery of at least 2 of 3 parameters needed to describe the bulk distribution of the generalized DSD. The third parameter can be prescribed by ground-based observations (Williams et al., 2014). Such measurements are important because increased knowledge of DSD factors improves the retrievals of rain rate and can be incorporated into numerical weather prediction (NWP) and climate models for increased performance and accuracy.

Fig. 4 illustrates an example of DPR's capability to probe vertical precipitation structure during a storm that occurred on October 31, 2022. In addition to the precipitation pattern near the surface, the DPR shows the vertical extent of the precipitation, including the melting layer, and high cloud tops indicated by the distinct reflectivity gradients from the Ku and Ka PRs.

During its decade of operation, much has been learned from GPM to advance the current understanding of the three-dimensional structure of precipitation systems, improve the global retrieval of precipitation, and enhance our understanding of the global water cycle. The DPR has served as the "anchor" for many of the advancements in the PMW algorithms and multisensor datasets and will continue to do so for the foreseeable future.

On April 16, 2023, the China Meteorological Administration launched its Feng Yun 3G (FY-3G) satellite, which carries a Ku/Ka-band precipitation measurement radar similar to GPM DPR. This new precipitation radar can further supplement low orbit precipitation measurements currently available from the international community.

Although not discussed in this chapter, there is a class of algorithms that use both the DPR and GPM Microwave Imager (GMI) where the data are coincident; these algorithms are the most accurate ones but have limited use because of the rather narrow swath width of the DPR.

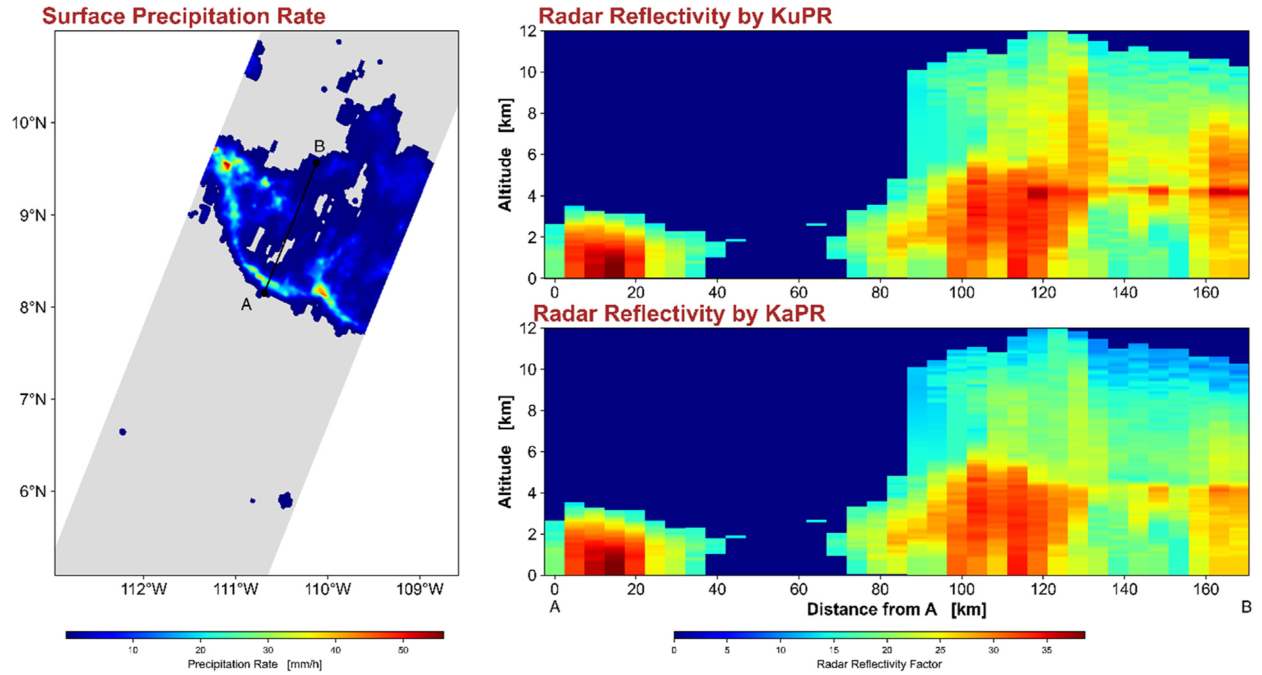

Fig. 4 GPM DPR observations and precipitation retrievals during a storm event at 10:40UTC, October 31, 2022. The surface precipitation rate estimates from DPR are shown on the left, whereas DPR vertical precipitation information (i.e., reflectivity) is shown on the right. The DPR reflectivity shows the vertical extent of the precipitation, including the melting layer.

RainCube

RainCube (Radar in a CubeSat) is a technology demonstration mission sponsored by NASA's Earth Science Technology Office (ESTO) In-Space Validation of Earth Science Technologies (InVEST-15) program (Peral et al., 2018; Sy et al., 2022). It was a joint development between the Jet Propulsion Laboratory and Tyvak NanoSatellite Systems (Tyvak). It was the first to successfully demonstrate novel precipitation radar technology at Ka-band (35.75 GHz) with a 50-cm diameter parabolic reflector antenna all fitting in a 6U CubeSat platform. The peak transmit power of RainCube's radar is 10 W, and it has a sensitivity of 12 dBZ.

Like all the existing space-based precipitation radars, RainCube was operated on a low Earth orbit from which it measured the vertical distribution of precipitation through the nadir-looking Ka-band radar. It was the only spaceborne precipitation radar that oversampled its measurements in the along-track direction. The horizontal resolution of RainCube measurement is 10 km, and the vertical resolution is 250 m.

RainCube was launched from the International Space Station in July 2018 and deorbited in December 2020. The success of RainCube has demonstrated the feasibility of cost-effective constellation missions of miniaturized radars in near-earth orbits for global 3-D measurements of precipitation (Sy et al., 2022).

Visible and Infrared Methods

This section provides an overview of visible (VIS) and infrared (IR) retrieval techniques, including the fundamental physics and assumptions that are applicable, and a number of VIS and IR-based precipitation and microphysical retrieval algorithms that are commonly used in the scientific community. VIS and IR were the first to be conceived for precipitation retrieval as these were the first sensors on the early weather satellites that date back to 1960s. Many of these methods are rather simple to apply while at the same time they show a relatively low degree of accuracy, and typically focus on rain rather than all forms of precipitation. On the other hand, GEO weather satellite VIS and IR imagers uniquely provide the rapid temporal update cycle (e.g., 10 min or less) needed to capture the growth and decay of precipitating clouds, with the most recent class of GEO satellites (i.e., GOES-R series; Schmit et al., 2017) providing a regional update capability of every 60 seconds (or 30 seconds if the two mesoscale domains are the same).

A complete overview of the early work and physical premises of VIS and thermal IR (10.5−12.5 μm) techniques is provided by Barrett and Martin (1981); while Kidder and Vonder Haar (1995) present some of the techniques that have evolved nearly 15 years later. The rainfall retrieval in these wavelengths is based on the fact that visibly bright (optically thick) clouds are positively correlated with regions of convective rainfall (Woodley and Sancho, 1971). On the other hand, clouds with cold tops in the IR imagery produce more rainfall than those with warmer tops (Scofield, 1987). However, the correspondence between cold tops and visible bright spots is far from perfect and cold cloud tops are not always well correlated with surface rainfall, especially in warm stratiform rainfall regimes. **Fig. 5** presents an example of composite VIS imagery from NOAA-21, formerly known as Joint Polar Satellite System – 2 (JPSS-2) prior to launch. The precipitation estimates from NASA's Integrated Multi-satellitE Retrievals for GPM (IMERG) on the same day are also indicated in **Fig. 5** to highlight VIS signatures associated with precipitation. **Fig. 6** illustrates an example of IR image from the advanced baseline imager (ABI) aboard the Geostationary Operational Environmental Satellite (GOES-16) during Hurricane Bonnie as it approached Clarion Island.

Various approaches have been developed to emphasize particular aspects of the sensing of cloud physics properties to reconcile differences between VIS and IR retrievals and measured rainfall. From a traditional standpoint, following Barrett and Martin's classification, the rainfall estimation methods can be divided into the following categories: cloud-indexing, bi-spectral schemes, life history, and cloud model-based. However, more recent advances over the past two decades have led to multispectral (e.g., VIS/IR) algorithms, machine learning models, as well as cloud microphysical techniques to retrieve actual cloud properties which can then be associated with various precipitation types. The following subsections provide details and examples of these VIS and IR precipitation retrieval techniques.

It should be noted that in many cases, the algorithms described could be fit into more than one category and that over time, more techniques could be considered "hybrid" approaches of these generalizations. Finally, it would be impossible to cite every noteworthy algorithm ever developed; it is the aim of this section to highlight examples to offer the readers some basic fundamentals of visible and IR precipitation retrieval.

VIS and IR Fundamentals

Although some of these concepts may appear in other parts of this volume, a few basic concepts of VIS and IR remote sensing are provided here for completeness. A good reference is Petty (2006), however, any book dedicated to atmospheric radiative transfer will provide similar information. This chapter will focus on some conceptual ideas without diving too much into the mathematical details or complex interactions between radiation and surface/atmospheric composition. In terms of the electromagnetic spectrum, gamma rays are the shortest wavelengths, followed by X-rays, ultraviolet, visible (~0.40–0.75 μm), near IR (~0.75–2.5 μm), IR (up to 1000 μm or 1 mm), MW (1 mm to 10 cm), and radio waves. For precipitation remote sensing, we rely on VIS, near IR, IR, and MW energy.

Radiation from the Earth's surface and from layers of the atmosphere is transmitted through the atmosphere to reach the satellite. For VIS, the satellite measures the reflection of solar energy by the surface and for the case of precipitation, it is the reflection of the cloud tops that the satellite measures. In general, the higher the cloud tops, the brighter the signal is. Other factors include the composition of the clouds: ice clouds tend to be more reflective than clouds that have just liquid droplets. Other atmospheric constituents like aerosols can affect the energy through a scattering process.

For IR, it becomes more complicated because we measure Earth emitted energy from various gaseous absorption bands that exist from oxygen, ozone, carbon dioxide, etc. Thus, in addition to effects from the underlying surface, which emits energy at different levels of efficiency (i.e., a surface that emits all of the energy that it absorbs is referred to as a "black body"—most clouds act as black

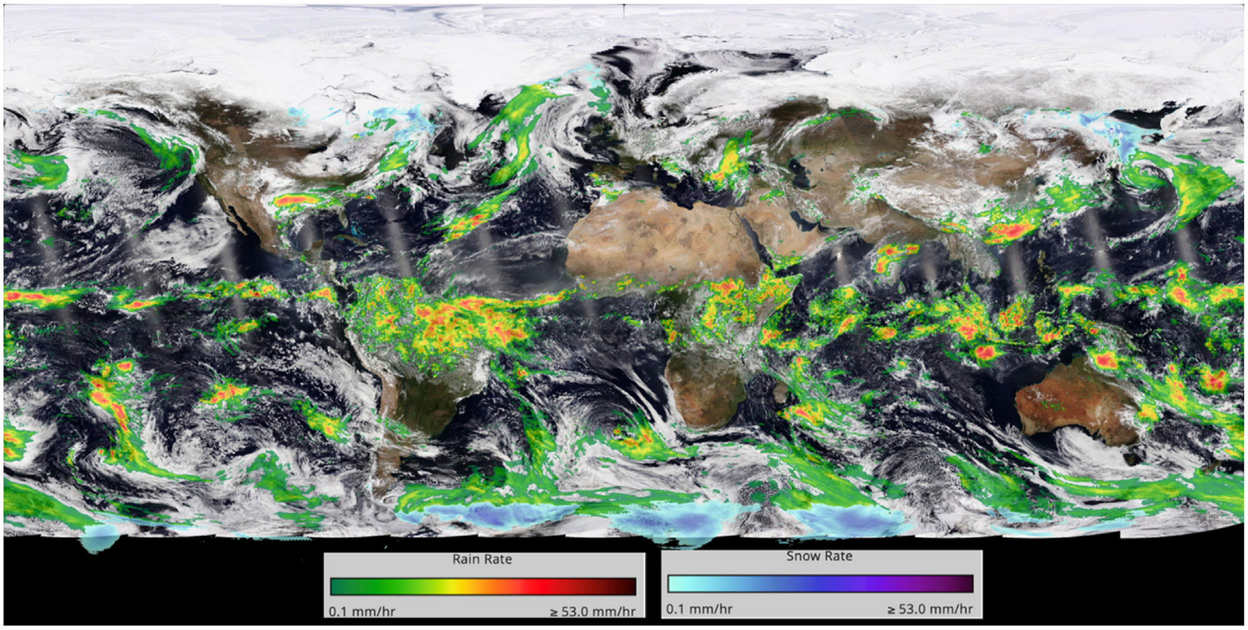

Fig. 5 NOAA-21 (designated JPSS-2 prior to launch) color composite visible imagery from April 20, 2024. The color maps indicate precipitation estimates from NASA's Integrated Multi-satellitE Retrievals for GPM (IMERG).

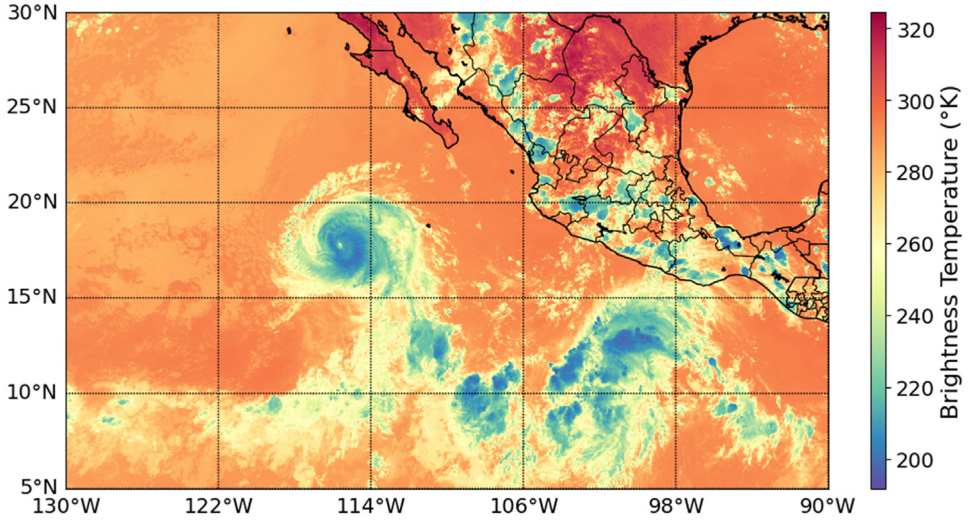

Fig. 6 Color enhanced infrared (IR) image from GOES-16 advanced baseline imager (ABI) channel 14 at 2130UTC on July 7, 2022. The higher cloud tops as inferred from IR temperatures are color enhanced in blue, indicating regions of deeper convection. Note the higher level clouds associated with Hurricane Bonnie as it approaches the Clarion Island (18.36°N, 114.73°W).

bodies), the temperature structure of the atmosphere also contributes to the satellite measurement. In fact, there is a class of IR sensors known as "sounders" that are specifically designed to exploit these absorption properties to retrieve the vertical profile of the atmosphere; such measurements are a critical component in NWP models.

Cloud-Indexing Methods

Cloud-indexing techniques assign a rain rate level to each cloud type identified in the satellite imagery. The simplest and perhaps most widely used is the one developed by Arkin (1979) during the Global Atmosphere Research Program's (GARP) Atlantic Tropical Experiment (GATE) on the basis of a high correlation between radar-estimated precipitation and fraction of the area colder than 235 K in the IR. The scheme, named the GOES Precipitation Index (GPI) (Arkin and Meisner, 1987), assigns these areas a constant rain rate of 3 mm h^{-1}, which is appropriate for tropical precipitation over 2.5° latitude × 2.5° longitude areas. The GPI became a standard for climatological rainfall analysis (e.g., Arkin and Janowiak, 1991) and is regularly applied and archived for climatological studies and monitoring of tropical precipitation, including seasonal changes related to equatorial Pacific sea-surface temperature warming and cooling episodes and Madden-Julian Oscillations (MJO) (Janowiak and Xie, 1999).

A family of cloud-indexing algorithms was developed at the University of Bristol. "Rain days" are identified from the occurrence of IR brightness temperatures (TB) below a threshold at a given location. The estimated rain days are combined with rain-per-rain day means that are spatially variable to produce rainfall estimations for extended periods (10 or more days). The most evolved version of the Bristol technique uses variable IR rain/no-rain TB thresholds (Todd et al., 1995, 1999). Another cloud-indexing method was developed for use in South America, where mesoscale convective complexes (MCC) are prevalent (Vila et al., 2008).

Bispectral Methods

Bi-spectral methods are based on the very simple, although not always accurate, relationship between cold and bright clouds and high probability of precipitation, which is characteristic of cumulonimbus clouds. Lower probabilities are associated with bright but warm clouds. The RAINSAT technique (Lovejoy and Austin, 1979; Bellon et al., 1980) screens out cold but not highly reflective clouds or those that are highly reflective but have a relatively warm top. The number of false alarms of the pure IR techniques is reduced. The algorithm is based on a supervised classification trained by ground radar to recognize precipitation from both VIS brightness and IR brightness temperature.

Life-History Methods

A family of techniques that specifically requires GEO satellite imagery because of its rapid update cycle is the life-history methods that rely upon a detailed analysis of the cloud's life cycle, which is particularly relevant for convective clouds. An example is the Griffith-Woodley technique described in Griffith et al. (1978). In this case, the increasing cloud area over time is treated differently from shrinking clouds. A major problem arises in the presence of high cirrus anvils from neighboring clouds: they often screen the cloud life cycle underneath leading to possible underestimates early in the day and overestimates toward the evening when, at least over many land areas, clouds mature and tend to produce larger areas of high cirrus. Reasonable performance of this method is obtained for deep convective storms, while contradictory results arise from their application to stratiform systems or weak convection. More recently, Bellerby (2004) adopted a feature-based approach and a cloud motion method (Bellerby, 2006) to derive rainfall from GEO measurements.

Cloud Model-Based Techniques

Cloud model techniques aim at introducing the cloud physics into the remote sensing retrieval process for a quantitative improvement that derives from the overall better physical description of the precipitation formation processes. A one-dimensional cloud model relates cloud-top temperature to rain rate and rain area using a convective stratiform technique (CST) to separate different forms of precipitation in convective and stratiform regions (Adler and Negri, 1988). Local minima in the IR brightness temperature are identified and screened to eliminate thin, nonprecipitating cirrus. To accomplish this, a slope parameter is calculated for each temperature minimum. Adler and Negri (1988) established an empirical discrimination of thin cirrus in the temperature/slope plane using radar and visible imagery data. If the temperature minimum and its slope falls to the left of the discrimination line, the temperature minimum location is classified as thin cirrus (nonraining). A larger slope implies a more clearly defined minimum that corresponds to a thunderstorm.

The first space-based lightning sensor was flown on the TRMM satellite, which offered a full gamut of observations for precipitation detection through combining the Lightning Imaging Sensor (LIS) with other payloads, including the visible and IR scanner (VIRS). Xu et al. (2013a,b) improved the CST through using the LIS information for better definition of convective cores. This work can potentially be extended for lightning sensors such as the Geostationary Lightning Mapper (GLM) which is now operating on the GOES-R series.

Multispectral Methods

As sensors became more sophisticated on GEO satellites, e.g., more spectral bands, higher temporal and spatial resolution, their combination were exploited in the next phase of GEO-based retrieval algorithms that were geared for QPE over relatively short time intervals. Some examples include the use of NWP moisture corrections for orographic driven precipitation (Vicente et al., 1998). Specifically, the digital elevation model (DEM) and low tropospheric winds are used to adjust the final retrievals (Vicente et al., 2002). The Auto-Estimator technique (Vicente et al., 1998) proposed a moisture correction factor (PW—RH) defined as the product of precipitable water (PW) in the layer from the surface to 500 mb multiplied by mean relative humidity (RH) data between the surface and the 500-mb level. The PW—RH factor decreases rainfall rates in very dry environments and increases them in very moist ones. The operational version of this algorithm, called Hydro-Estimator (HE), uses PW to adjust the power-law relation between cloud-top temperature and precipitation rates, while RH is applied to adjust the final rain rates (Scofield and Kuligowski, 2003; Kuligowski et al., 2016). **Fig. 7** presents an example of GOES-16 IR-enhanced images from ABI channel 8 and channel 14, as well as the corresponding rain rate estimates at 2200 UTC on January 13, 2024.

The GOES Multi-spectral Rainfall Algorithm, GMSRA (Ba and Gruber, 2001), combines multispectral measurements of the GEO satellites to estimate rainfall. One of the principal innovations of GMSRA relative to previous IR/VIS algorithms is that it combines several cloud properties used in a variety of techniques in a single and comprehensive rainfall algorithm. In particular, this technique uses cloud-top temperatures as a basis of rain estimation (e.g., Arkin and Meisner, 1987; Vicente et al., 1998), and it utilizes the effective radii of cloud particles (e.g., Rosenfeld and Gutman, 1994) and spatial and temporal temperature gradients (e.g., Adler and Negri, 1988; Vicente et al., 1998) to screen out nonraining clouds.

Kuligowski (2002) built upon the framework of the HE to develop the Self-Calibrating Multivariate Precipitation Retrieval (SCaMPR) algorithm to exploit the rapid update available from GEO satellites and the more direct measure of precipitation from PMW sensors. In its current form (Kuligowski et al., 2013, 2016), SCaMPR uses GOES bands 3 (6.7 μm) and 4 (10.7 μm) brightness temperatures (and the difference between the two) as predictors, plus a pair of measures of local texture of the GOES band 4 field. These predictors are calibrated against the Climate Prediction Center (CPC) combined microwave (MWCOMB) data set. With the launch of GOES-16 in 2016, this algorithm now uses predictors from two water vapor bands (6.2 and 7.3 μm) and the IR window bands at 8.5, 10.8, and 12.0 μm, which will enhance its skill at detecting thin cirrus and rain from warmer clouds.

Cloud Microphysical Retrieval Techniques

Exploitation of visible and near-IR bands can infer information on cloud microphysical properties, specifically, cloud droplet and ice particle sizes. These techniques can be limited when cirrus clouds obscure the particles below which are related to precipitation processes and in some cases, to daytime observations where reflected solar energy is needed. Nonetheless, these methods have shown value for specific, regional applications where the precipitation characteristics can be adequately characterized by cloud microphysical properties. Advancement in sensors (i.e., more channels, higher spatial resolution) has given these techniques more significance over time.

Some of the early work was noted by Rosenfeld and Gutman (1994), who utilized multispectral measurements from the Advanced High Resolution Radiometer (AVHRR) to retrieve rain associated with mid- and low-level clouds over arid regions. Recent work in this area includes Chen et al. (2008), who focused on maritime light rain and drizzle associated with stratus clouds; Cattani

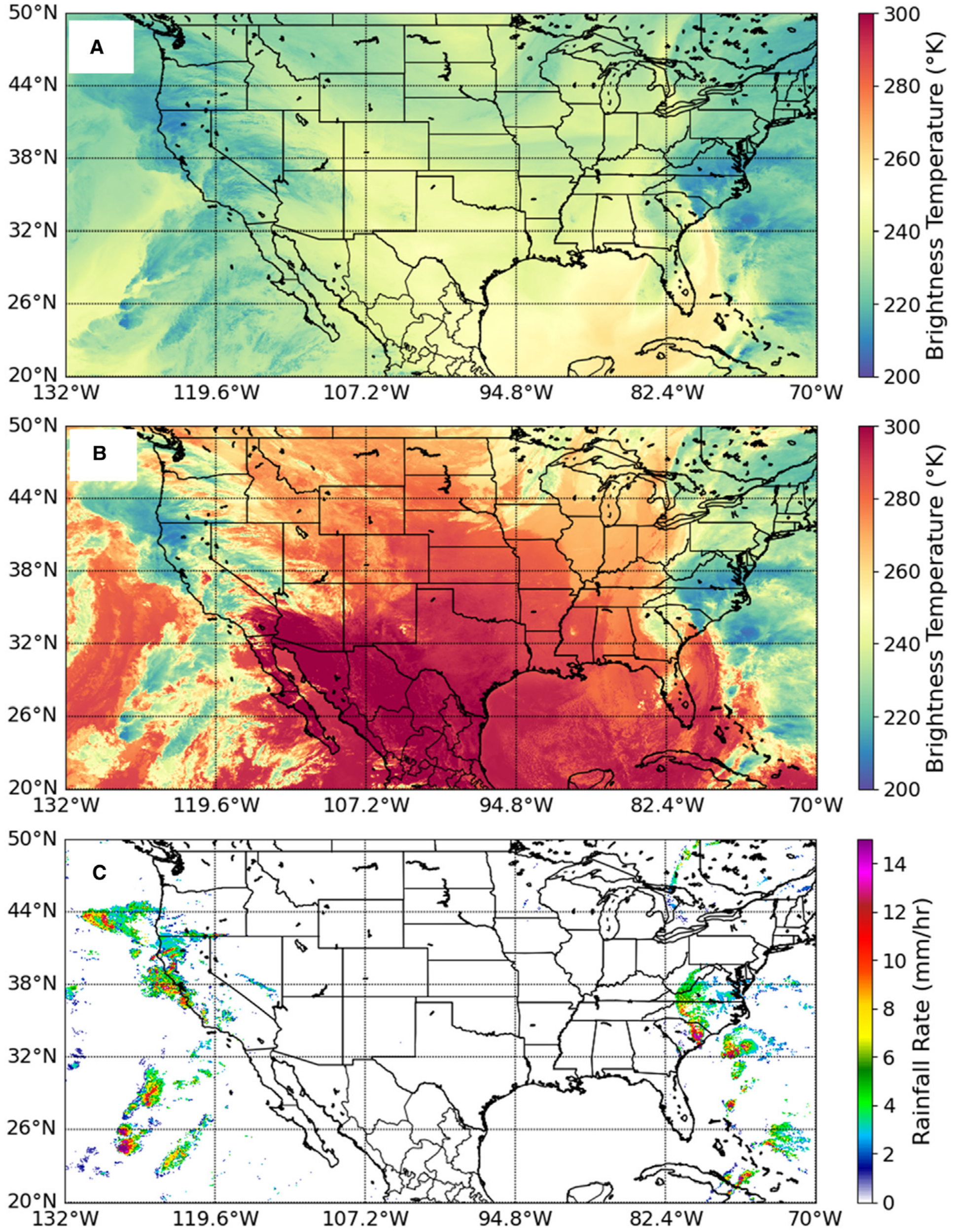

Fig. 7 GOES-16 IR images from ABI channel 8 (top) and channel 14 (middle), as well as corresponding rain rate estimates (bottom) for 2200 UTC on January 13, 2024. The rain region identified over California was associated with an extreme precipitation event known as an Atmospheric River.

et al. (2009), who focused on Mediterranean convective complexes; Walther and Heidinger (2012), who developed global methods to retrieve both liquid and ice particle information; Ehsani et al. (2021), who used machine learning to retrieval snowfall in high latitude based on AVHRR measurements.

Passive Microwave (PMW) Methods

In this section, passive microwave (PMW) satellite retrieval techniques for precipitation are reviewed. Unlike VIS and IR signals, microwave energy can penetrate clouds, and depending on the frequency, can sense near surface precipitation. PMW sensors with channels 6–190 GHz are highly sensitive to precipitation articles. This direct impact on microwave measurements by hydrometeors allows for the quantitative detection of precipitation properties in the atmosphere as well as on the surface. It should be pointed out that “passive” means naturally emitted radiation from the Earth’s surface and atmosphere that interacts with clouds and precipitation and is detected by a radiometer on-board a satellite. Unlike the active sensors (i.e., radars) that transmit electromagnetic waves, PWM sensors do not have transmitters.

There are three major techniques in precipitation estimation using passive microwave radiometry, namely, emission-based methods, scattering-based methods, and physically based methods, which will be discussed following a brief overview of the physics underlying PMW retrievals.

PMW Fundamentals

Unlike the VIS and IR, microwave radiation can be more complex because the surface is not a blackbody. Because microwave energy is at longer wavelengths, it can see through many types of clouds that hinder the VIS and IR, thus providing a more all-weather capability. Here we will focus on passive MW, which is energy naturally emitted by the Earth and atmosphere, as shown in Fig. 8. Active MW is more complicated, although only so when precipitation is present. A good reference for passive MW can also be found in Petty (2006).

Most passive microwave radiometers for precipitation observation launched to date operate in frequencies ranging from 6 to 190 GHz. In this frequency range, microwave radiometers observe different parts of the precipitation profile. Below 20 GHz, emission by precipitation-size rain drops dominates and ice particles above the rain layer are nearly transparent. Above 60 GHz, ice scattering dominates, and the radiometers cannot sense the rain drops below the freezing layer. Both emission and scattering effects are important for frequencies between 20 and 60 GHz. In general, over oceans, emission by liquid drops raises brightness temperature while scattering by ice particles has the opposite effect. Besides the shift in the dominating mechanism from emission to scattering with the increase of frequency, rain rate also plays a role by enhancing both the emission and the scattering signals. It is noted that the scattering by ice increases much more rapidly with frequency than scattering by liquid (Gasiewski, 1993; Kidder and Vonder Haar, 1995). Window channels can measure down to the earth's surface and are strongly influenced by surface properties (i.e., vegetation, soil moisture, etc.) (Ferraro et al., 1994, 2013). Other frequencies are sensitive to oxygen or water vapor/cloud droplets absorption. And during the past two decades, frequencies at or above 90 GHz have proven to be useful for the retrieval of snowfall (i.e., Kongoli et al., 2015; Skofronick-Jackson et al., 2018). These microwave properties set the foundation for the development of PMW precipitation estimation schemes.

PMW Emission-Based Methods

PMW emission-based rainfall algorithms are mostly applicable over ocean because water surfaces are relatively homogeneous and provide a cold background due to low emissivity. Below certain threshold rain intensity, emission dominates rather than scattering over water especially at lower frequencies. Brightness temperature (TB), which is directly related to the measured radiance, increases rapidly with rain rate in this range and provides the basis for many emission-based precipitation retrieval methods. The primary disadvantage of emission-based techniques is that the microwave signal can saturate with moderate to heavy rain rates (which is frequency dependent), thus providing a strong nonlinear relationship between rain rate and TB. However, recent advances in sensor spatial resolutions, most notably on the NOAA JPSS ATMS and the GPM Microwave Imager (GMI), offer the opportunity to exploit measurements to retrieve high rain rates.

The earliest efforts to estimate rain rate from satellite measurements used microwave data from a series of NASA missions; this included the electrically scanning microwave radiometer (ESMR) on the Nimbus 5 and Nimbus 6 satellites and the scanning multichannel microwave radiometer (SMMR) on both Nimbus 7 and Seasat-A. Wilheit et al. (1977) employed a radiative transfer model to calculate the 19.35 GHz TB as a function of rain rate over ocean, and used the 19.35 GHz measurements from ESMR-5 to retrieve rain rate. These sensors had vertically and horizontally polarized channels and Weinman and Guetter (1977) utilized the weak

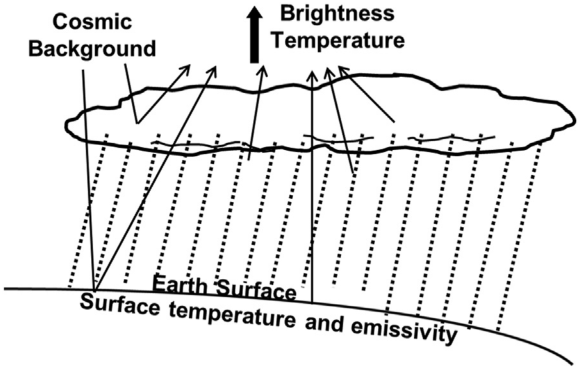

Fig. 8 Passive microwave remote sensing brightness temperature observations measure naturally emitted and/or scattered energy from the cosmic background, the surface temperature and emissivity, and the particles within the clouds. The resultant brightness temperature values are an integrated quantity throughout the vertical column and are expressed in Kelvin.

polarization of 37 GHz radiances from ESMR-6 to discriminate convective rain over land from open water. Rain rate over water was expressed as a function of TB taking into consideration the polarization effects; a lower polarization was correlated to heavier rain rates. SMMR had five frequencies with both horizontal and vertical polarizations. Spencer et al. (1983) took advantage of the significant impact of rain drops on the thermal emission at lower frequencies (highest SMMR frequency is 37 GHz) and used multiple regression approach to relate SMMR TB's to rain rate.

The first of the Special Sensor Microwave/Imager (SSM/I) series was launched in 1987 and was followed by five more successful SSM/I instruments, and then a follow on sensor, the SSMIS, which has flown on four satellites and is still in operation today. The SSM/I has seven channels: y and horizontally polarized channels at 19.35, 37.0, and 85.5 GHz and vertically polarized channel at 22.235 GHz; the SSMIS expands to 24 channels that combines several capabilities, including temperature and moisture retrievals (of significance to precipitation retrieval is the inclusion of channels at 150 and 183 GHz; the 85.5 GHz channel is replaced by 91.6 GHz). The SSM/I is a well-studied instrument for rainfall estimation. Ferraro and Marks (1995) developed an SSM/I algorithm linking oceanic rain rate with liquid water path (Weng and Grody, 1994) using ground-based radar measurements. The retrieval of liquid water path relies on the emission signatures at 19 and 37 GHz.

Mugnai and Smith (1984) were the first to combine the cloud model with the radiative transfer model for estimating TB's from convective clouds. Studies along this line of thinking followed (Olson, 1989; Smith et al., 1994). The Goddard profiling algorithm (GPROF) is one of the inversion algorithms that computes radiative transfer based on output from cloud models (Kummerow et al., 1996, 2001; Pfreundschuh et al., 2024). GPROF was applied to the TRMM Microwave Imager (TMI) (in orbit 1997–2015) for the retrieval of surface rain rate and rainfall profile. A large a priori database of atmospheric profiles and TB at the TMI frequencies was constructed using output of two cloud-resolving models and a one-dimensional radiative transfer model. Then the algorithm utilizes a Bayesian inversion approach to derive instantaneous rain rate and rainfall profile by a weighted summation of all the profiles in the database. The weight is determined by how close each TB vector in the database resembles the observed vector. GPROF is also the primary rainfall algorithm being applied to the Advanced Microwave Sounding Radiometer-Earth Observing System (EOS) (AMSR-E) (Wilheit et al., 2003). GPROF has undergone several changes over the past decade to make it more robust for use on multiple satellites, to include more diversity in the databases, and to expand its utility for both rainfall and snowfall (e.g., Gopolan et al., 2010; Meyers et al., 2015; Kummerow et al., 2015).

Fig. 9 illustrates some emission signatures over the ocean due to clouds and precipitation from the NOAA-21 ATMS sensor. Going from the lower frequencies at 31.4 GHz up to 183.3 GHz, greater sensitivity to precipitation and clouds can be seen by the warming signatures compared with the radiatively cooler ocean surface. Use of multiple channels that are sensitive to both non-raining and raining clouds can provide the full dynamic range of precipitation. Note that there are many other features unrelated to precipitation noted in the imagery, such as sea-ice, water vapor over ocean, and different surface types over land.

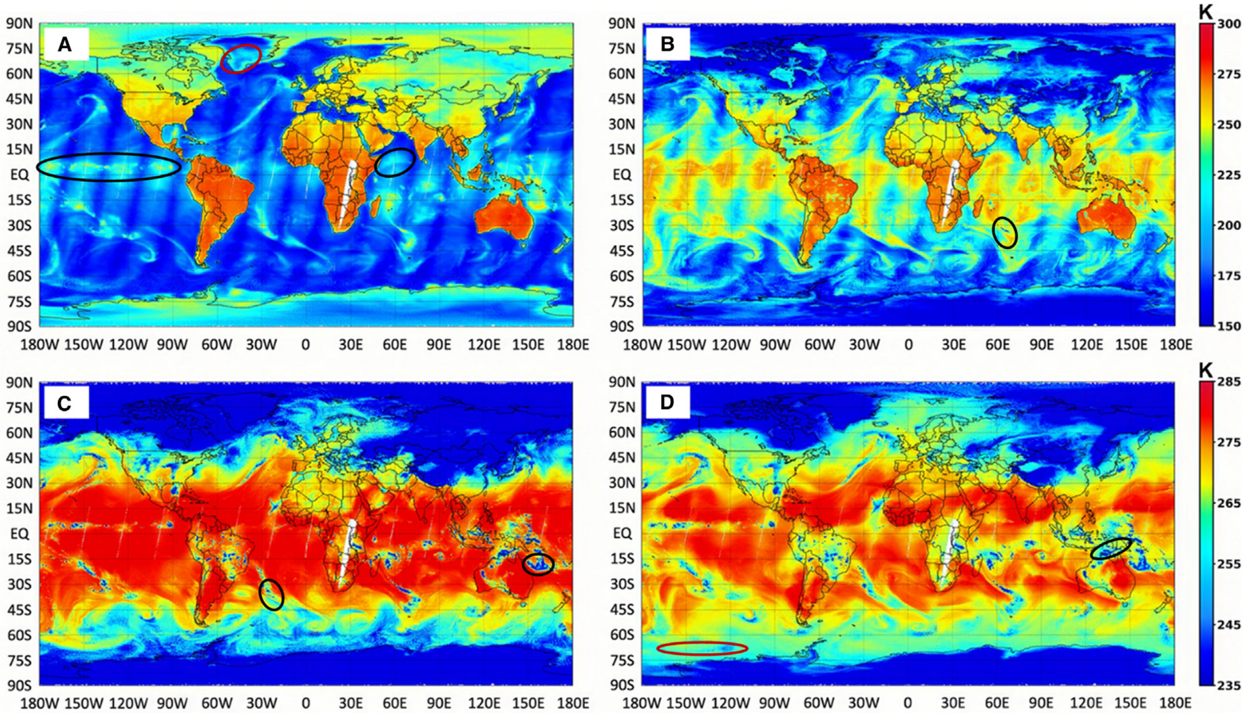

Fig. 9 NOAA-21 ATMS descending overpasses on January 23, 2024. (A)–(D) are brightness temperatures at 31.4 GHz (channel 2, vertical polarization), 88.2 GHz (channel 16, vertical polarization), 165.5 GHz (channel 17, horizontal polarization), and 183.31 GHz (channel 18, horizontal polarization), respectively. Examples of features related to liquid precipitation are highlighted by the black ovals and those related to solid precipitation are indicated by red ovals.

PMW Scattering-Based Methods

Due to the higher, but more varying emissivity of the land surface, in the past the only reliable means of detecting precipitation over land was by isolating depressed TB's as a result of scattering by millimeter sized ice particles that exist in most rain clouds. Since the signal being captured is predominantly a result of ice particles (including snowflakes) instead of rain drops, the scattering-based precipitation estimation is an indirect measure, as it relates the magnitude of the scattering at and above the freezing layer to surface precipitation. The launch of the SSM/I in 1987 provided the first opportunity to retrieve rain rate through scattering at higher frequency (85 GHz). Meteorological satellites launched since then have included channels at or above 85 GHz that are sensitive to scattering, including more recent sensors that contain measurement channels at or above 150 GHz. Thus, these measurements have been exploited to develop scattering-based precipitation algorithms since they are sensitive to snowfall as well. These include the SSMIS, AMSU-B/MHS, TMI, and GMI sensors.

Spencer et al. (1989) first introduced the concept of polarization-corrected brightness temperature (PCT) which is a linear combination of the vertically and horizontally polarized brightness temperatures at 85.5 GHz. The coefficients in PCT can be adjusted so that PCT is only sensitive to the scattering in the upwelling microwave radiation but not to other atmospheric and land surface conditions including the contrast of land vs. ocean.

An operational SSM/I rain rate product generated at Fleet Numerical Meteorology and Oceanography Center (FNMOC) (Ferraro, 1997) combines a scattering-based global algorithm with the earlier-mentioned SSM/I emission-based ocean algorithm (Ferraro and Marks, 1995). The global algorithm calculates a scattering index (SI) (Grody, 1991) which is the difference between the vertically polarized 85.5 GHz observation and an estimate of the nonscattering contribution from this channel. The latter is a linear combination of the observations at lower channels (19.35 and 22.235 GHz). The SI algorithms are calibrated with ground-based radar measurements to produce instantaneous rain rate for both ocean and land (Ferraro and Marks, 1995). The emission-based algorithm complements the SI algorithm by detecting rain systems over ocean that have little or no ice scattering. A decision tree is included in the algorithm to screen out surface scattering sources such as snow cover and desert. This widely used algorithm was also adapted into the TRMM GPROF land rain rate algorithm as described by McCollum and Ferraro (2003). The relationships between rain rate and 85 GHz brightness temperature are recalibrated using TRMM precipitation Radar (PR) data, and a new procedure is developed to estimate convective rainfall. Subsequent improvements to this adaptation included Gopolan et al. (2010) and Meyers et al. (2015). **Fig. 9**B (88.2 GHz) illustrates some scattering signatures over land associated with convective storms.

The first operational sensor with readily available data above 89 GHz was the Advanced Microwave Sounding Unit (AMSU-B) which was flown on the NOAA-15 satellite in 1998. AMSU-B has operated on three satellites and was replaced with a similar sensor, the Microwave Humidity Sounder (MHS), which continues to operate on NOAA-18 and NOAA-19, as well as MetOp-A, -B, and -C. The MHS has recently been relaced by the Advanced Technology Microwave Sounder (ATMS), which is a 22-channel scanning microwave radiometer and has been flown on the Suomi NPP and the Joint Polar Satellite Systems (i.e., NOAA-20 and -21).

Zhao and Weng (2002) took advantage of the highly scattering nature of 89 and in particular 150 GHz radiances from the AMSU-B and retrieved ice water path (IWP) using scattering parameters measured at these two channels. The derived IWP is then converted into the surface rainfall rate through an IWP and rainfall rate relationship developed from cloud model results (Weng et al., 2003). The algorithm was further refined, including the use of the 183 GHz water vapor bands to delineate regions of deep convection, as described in Ferraro et al. (2005) and Vila et al. (2008), and runs as an operation rain rate product at the NOAA National Environmental Satellite, Data, and Information Service (NESDIS).

To illustrate the signatures associated with precipitation from the high frequencies, **Fig. 10** shows the brightness temperatures at 88.2, 165.5, and 183.31 ± 7 GHz from the NOAA-20 ATMS. As we focus on the storm system over southeast US and adjacent ocean regions, there is generally a warmer signature compared with the ocean background at 88 GHz that is associated with the rain region due to emission processes. At 165 GHz, these features now show up as cold signatures, and extend over land; these are strictly due to scattering due to precipitation sized ice particles. There are five bands on ATMS in the 183 GHz water vapor regime; in **Fig. 10**, we highlight 183 ± 7 GHz. Although water vapor signatures are dominate in the image (note the warm features stretching across the United States), there are pockets of colder TB's in the precipitation region; these indicate deeper convective precipitation features, where the ice extends above 6 km.

Since the original work of Zhao and Weng (2002), several other precipitation algorithms emerged from the AMSU/MHS sensors; this includes the Microwave Integrated Retrieval System (MiRS; Boukabara et al., 2011; Boukabara et al., 2013; Liu et al., 2020), the 183-WSL algorithm used by EUMETSAT (Laviola and Levizzani, 2011; Laviola et al., 2013), a MW radiometer constellation approach used by GPM (Kidd et al., 2016), and most recently a machine learning approach to improve the MiRS precipitation retrievals (Liu et al., 2023).

PMW Physically Based Methods

Radiometer algorithms for uniform global precipitation estimates must be physically consistent across multiple frequencies and sensors. Bayesian or Optimal Estimation algorithms are well suited to retrieve precipitation and its vertical structure by comparing the information content of any multifrequency radiometer to that supplied by a common a priori database of vertical profiles of precipitating clouds together with simulated brightness temperatures for each profile and sensor. By associating precipitation by spaceborne radar (as truth) and PMW brightness temperatures (as observed), a robust global a priori cloud database constrained

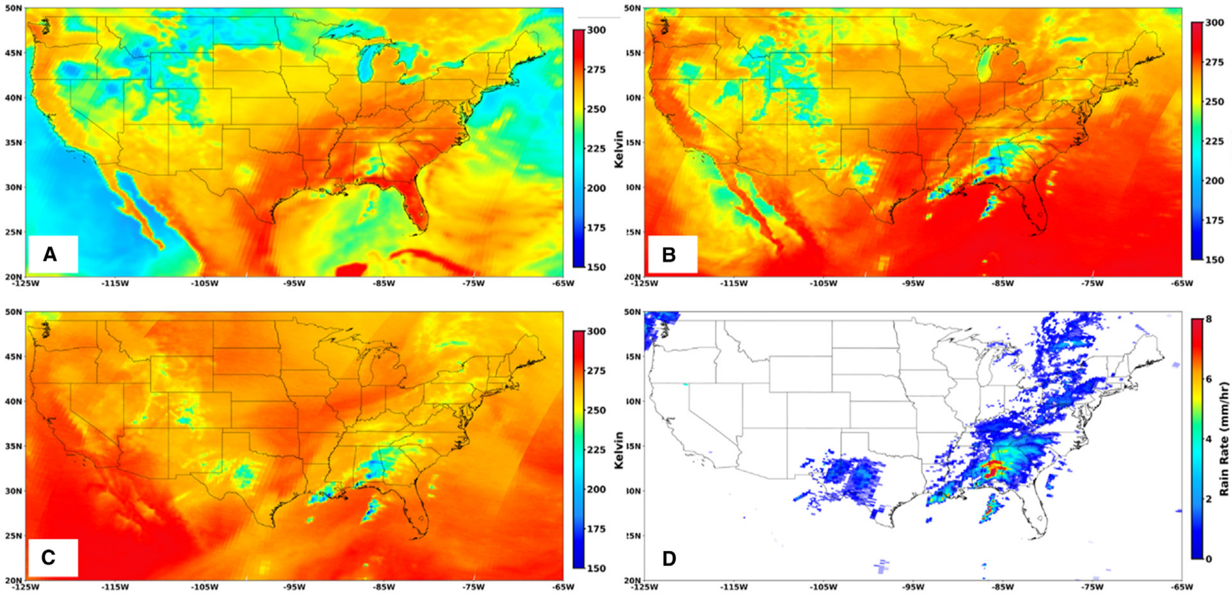

Fig. 10 NOAA-20 ATMS descending overpasses on November 25, 2022. (A)—(C) are brightness temperatures at 88.2 GHz (channel 16), 165.5 GHz (channel 17), and 183.31 GHz (channel 18), respectively. (D) shows the corresponding MiRS retrieved rain rates.

by both DPR and GMI measurements can be constructed. This eliminates the need for a priori databases that rely solely on cloud-resolving models as described in emission-based methods (Fig. 11). This approach, designated as "radar-enhanced" radiometer algorithms, improves accuracy and physical consistency. The methodology can be used over both land and ocean surfaces by creating separate a priori databases associated with similar land climatology classifications (Kummerow et al., 2015). This observationally and physically based a priori Bayesian retrieval is the methodology employed by TRMM in its later algorithms and by GPM currently. Algorithms in this form also have the capability to transition into truly physically based retrievals by incorporating the physical characteristics of surface properties and using that to retrieve surface emissivity for use instead of the land climatology classifications as currently employed (Ferraro et al., 2013; Boukabara et al., 2013; Ringerud et al., 2015).

Multisensor Precipitation Datasets

The individual sensors and retrieval approaches discussed so far each have limitations which make them unsuitable for use in certain situations; their utility is driven by the need of a particular user, e.g., a weather forecaster or a climate scientist or a particular observational need. For instance, from a satellite remote sensing perspective, frozen and mixed precipitation may be of more interest in the mid-latitudes and very light rain and snow may be of more interest over complex surface types in the polar regions. In addition, radar sensors directly observe precipitation particles, whereas PMW sensors indirectly observe integrated columnar precipitation characteristics. PMW estimates over the ocean might be more accurate than GEO-IR estimates, but the latter are better suited for studies of the diurnal cycle due to the superior temporal sampling obtained from a GEO satellite. For ground-based remote sensing observations, radars may be blocked by terrain or otherwise unable to observe precipitation features, necessitating the inclusion of other data sets such as satellite, rain gauge networks or numerical model forecasts to fill in the gaps. Conveniently, the available remotely sensed estimates of precipitation have different strengths and weaknesses, so that combined datasets can be superior to estimates from individual sensors. This section will present some evolution on this topic from both space-based and ground-based perspectives, and then highlight several very mature combined global precipitation products and their attributes.

As previously described, the advent of the first operational passive microwave sensors in the 1980s led to a surge in the development of various retrieval approaches. To foster collaborations among the community, and to determine which methods were perhaps more robust than others, several efforts to intercompare and evaluate various types of precipitation algorithms using remotely sensed information were carried out. The WetNet (Dodge and Goodman, 1994) Precipitation Inter-comparison Projects (PIP) evaluated multiple global and near-global precipitation algorithms including merged satellite datasets (Barrett et al., 1994; Kniveton et al., 1994; Smith et al., 1998; Adler et al., 2001). The Global Precipitation Climatology Project (GPCP) similarly sponsored three Algorithm Inter-comparison Projects (AIP; Ebert et al., 1996) that compared precipitation estimated from satellite observations against high-resolution observations from rain gauges and radars over limited domains (Arkin and Xie, 1994; Ebert and Manton, 1998). Among other results, these studies showed that PMW estimates were more accurate than IR estimates on an instantaneous basis, but algorithms which combine PMW and IR estimates were superior in terms of bias and standard errors. However, these intercomparisons did not show significant differences between individual algorithms of a common type and it remains the

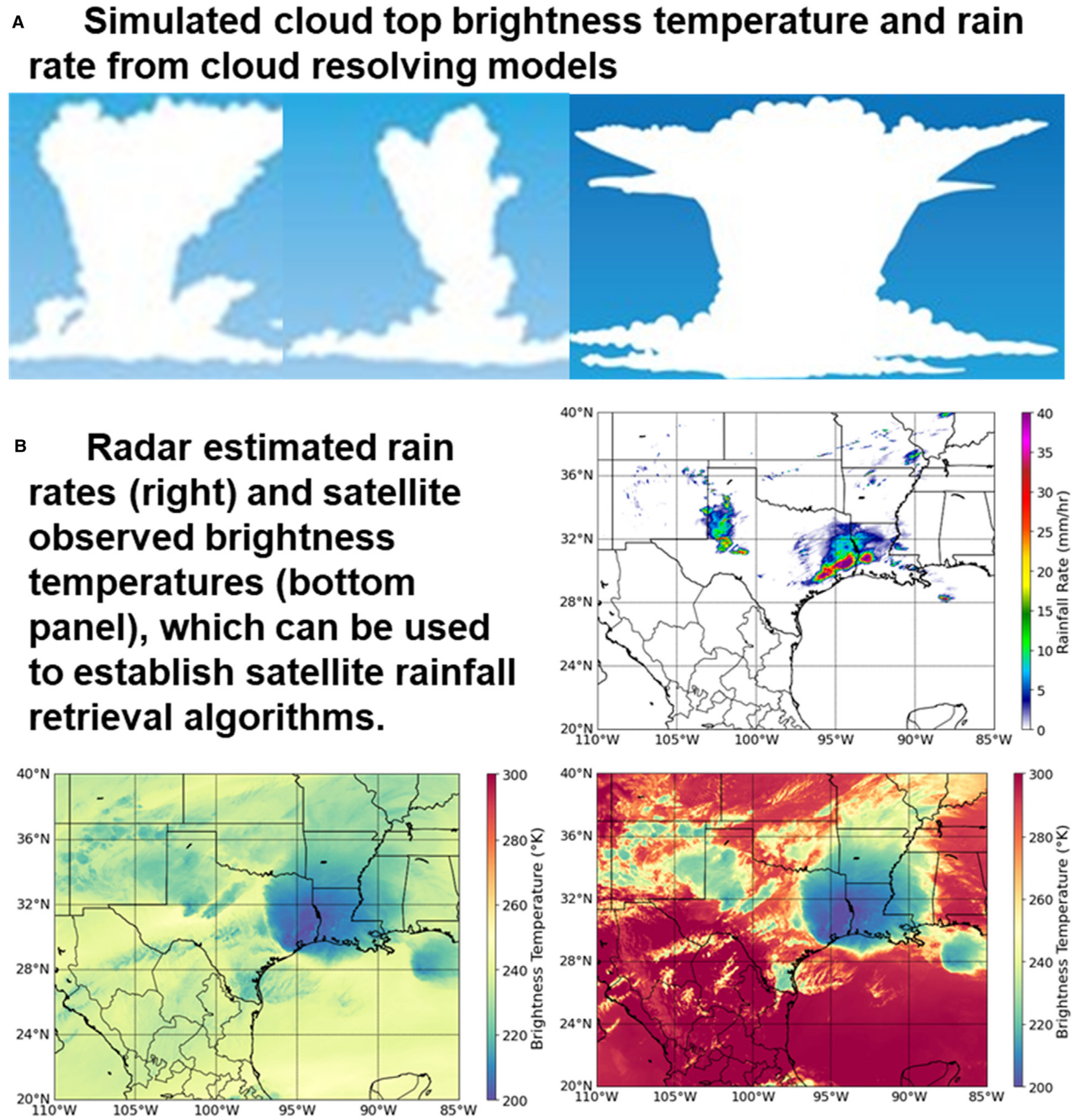
A Simulated cloud top brightness temperature and rain rate from cloud resolving models

B Radar estimated rain rates (right) and satellite observed brightness temperatures (bottom panel), which can be used to establish satellite rainfall retrieval algorithms.

Fig. 11 Conceptual comparison of (A) emission-based methods with (B) physically based PMW retrievals. Plots in (B) include ground-based radar rainfall rate estimates (upper panel) and corresponding BT observations from satellite. The emission-based methods are primarily based on simulated satellite observations and rain rates, while the methods in (B) are based on satellite PMW and active ground- or space-based radar observations.

case that several merged satellite products exist without a clear consensus on which is superior, and it is common to see a range of similar datasets used in the literature.

More recently, activities within the World Meteorological Organization (WMO) International Precipitation Working Group (IPWG; see Kidd et al., 2010) have established regular monitoring and validation of several satellite products, including many merged products (Ebert et al., 2007). Furthermore, under the auspices of IPWG, the Pilot Evaluation of High Resolution Precipitation Products (PEHRPP) was established to intercompare and validate these datasets. PEHRPP included a number of high-resolution datasets: the TRMM Multi-Satellite Precipitation Analysis (TMPA; Huffman et al., 2007), the CPC Morphing technique (CMORPH; Joyce et al., 2004), the Hydro-Estimator (Scofield and Kuligowski, 2003), the NRL-Blended technique (NRL-Blended; Turk and Miller, 2005), Precipitation Estimation from Remotely Sensed Information using Artificial Neural Networks (PERSIANN; Hsu et al., 1997), and the Global Satellite Mapping of Precipitation (GSMaP) project (Kubota et al., 2007). Studies to compare these datasets were carried out, although there is no technique that outperforms the others on a consistent basis (e.g., Ebert et al., 2007; Sapiano et al., 2008; Derin et al., 2019; Bytheway et al., 2023).

Table 2 provides attributes of several mainstream satellite precipitation datasets. Note that it is difficult to provide detailed error estimates for these products because of the varying temporal and spatial resolutions that they are produced. Additionally, there are regional differences among them (e.g., Maggioni et al., 2016; Bytheway et al., 2023, among others). Finally, there are also a host of statistical parameters that are important based on the application: for climate monitoring, bias is perhaps the most important whereas for hydrological applications, the root mean square error (RMSE) and correlation with in situ data are important. However, in general, these products have RMSE errors that range between 5 and 15 mm/day, depending upon the storm type and intensity (i.e., large scale systems have lower RMSE, whereas regional, convective systems have larger RMSE).

GPCP

Perhaps the most noteworthy blended precipitation product is the Global Precipitation Climatology Project (GPCP; Huffman et al., 1997; Adler et al., 2003; Huffman et al., 2009; Adler et al., 2018; Huffman et al., 2023a). Although GPCP has evolved into several versions over the years, including subdaily time scales, the baseline product is a global, 2.5-degree resolution monthly precipitation analysis beginning in 1979. The latest version of the GPCP monthly product is the version 3.2 dataset (Huffman et al., 2023a), which utilizes the Merged CloudSat, TRMM, and GPM (MCTG) climatological precipitation product over the mid-and high-latitude oceans (Behrangi and Song, 2020) and an updated Tropical Composite Climatology over the tropical oceans for climatological calibration (TCC, Adler et al., 2009; Wang et al., 2014), in order to improve performance of previous versions.

Although the monthly, 2.5-degree products are most commonly used, higher resolution products also exist as part of the GPCP suite. Noticeably, GPCP Version 1.3 is the first generation GPCP daily product to provide 1° gridded precipitation estimates over the entire globe from October 1996 to present (Huffman et al., 2023a). This daily product is created based on the One-Degree Daily (1DD) technique described in Huffman et al. (2001) and then calibrated to the GPCP Version 2.3 monthly product to ensure accuracy and consistency (Huffman et al., 2023a). The GPCP Version 3.2 also provides daily, global 0.5° gridded precipitation data covering June 2000 through September 2021, using the increased number of spaceborne sensors and enhanced merging algorithms in the GPM era. This daily product was calibrated using the new GPCP v3.2 monthly product and will eventually replace the GPCP Version 1.3 daily product.

CMORPH

NOAA's Climate Prediction Center (CPC) has developed a blended precipitation product known as CMORPH (CPC MORPHing technique), which produces global precipitation estimates at very high spatial and temporal resolution (Joyce et al., 2004; Xie et al., 2017). CMORPH uses precipitation estimates that have been derived from LEO PMW measurements, and whose features are transported via spatial propagation information that is obtained entirely from the more frequently updated GEO IR data This "morphing" feature makes the product unique from most of the other similar products described in this section. As is the case with GPCP, there are a number of CMORPH products at various time and spatial resolutions, however, the finest resolution

Table 2 Summary of merged satellite precipitation products and their attributes.

Product name	*Primary data sources*	*Spatial domain*	*Temporal and spatial resolutions*	*Period of record*
GPCP V1.3	GEO IR LEO PMW Rain gauges	90S–90N	Monthly—250 km Daily—100 km	1979–present 1997–Present
GPCP V3.2	GEO IR LEO PMW Rain gauges	90S–90N	Monthly—250 km Daily—50 km	1983–present 2000–Present
TMPA	GEO IR LEO PMW	50S–50N	3 hourly—25 km Daily—25 km Monthly—25 km	1998–2019
IMERG V07	GEO IR LEO PMW	90S–90N	30 min—10 km Monthly—25 km	2014–Present
CMORPH V01	GEO IR LEO PMW	60S–60N	30 min—8 km	1998–Present
CMORPH V02	GEO IR LEO PMW	90S–90N	30 min—5 km	1998–Present
PERSIANN	GEO VIS/IR LEO VIS/IR	60S–60N	1 hourly—25 km	2000–Present
GSMaP	GEO IR LEO PMW	60S–60N	1 hourly—10 km	1998–Present

of CMORPH version 1.0 is 30 minutes and 8 km, and the finest scales of CMORPH version 2.0 are at 30 min and 5 km. To achieve the finest spatial resolution, interpolation is performed (Xie et al., 2017; Chen et al., 2020).

In CMORPH, IR data are used as a means to transport, or morph, the microwave-derived precipitation features during periods when microwave data are not available at a location. Propagation vector matrices are produced by computing spatial lag correlations on successive images of geostationary satellite IR which are then used to propagate the microwave-derived precipitation estimates. This process governs the movement of the precipitation features only. At a given location, the shape and intensity of the precipitation features in the intervening half hour periods between microwave scans are determined by performing a time-weighting interpolation between microwave-derived features that have been propagated forward in time from the previous microwave observation and those that have been propagated backward in time from the following microwave scan (Joyce et al., 2004). Compared to version 1.0, the second generation of CMORPH (i.e., version 2.0) can not only provide higher resolution complete global coverage (90°S-90°N) with low production latency, but also greatly improves representation of cold season precipitation (Xie et al., 2023).

An example of accumulated precipitation from CMORPH, both version 1.0 and version 2.0, over the United States during an event in December 2023 is shown in **Fig. 12**A and B. Multiple regions of precipitation are indicated, including one shallow rainfall system in southern California and a massive storm (event total exceeding 160 mm) near the US Gulf Coast. It should be noted that the CMORPH products shown in **Fig. 12**A and B are near real-time (raw) products without any bias correction. In reality, the biased corrected CMORPH is often used for various applications, especially at long-term climate scale. The bias correction is based on probability density function (PDF) matching against the CPC daily gauge analysis over land and through adjustment against the GPCP merged analysis of precipitation over ocean (Xie et al., 2017).

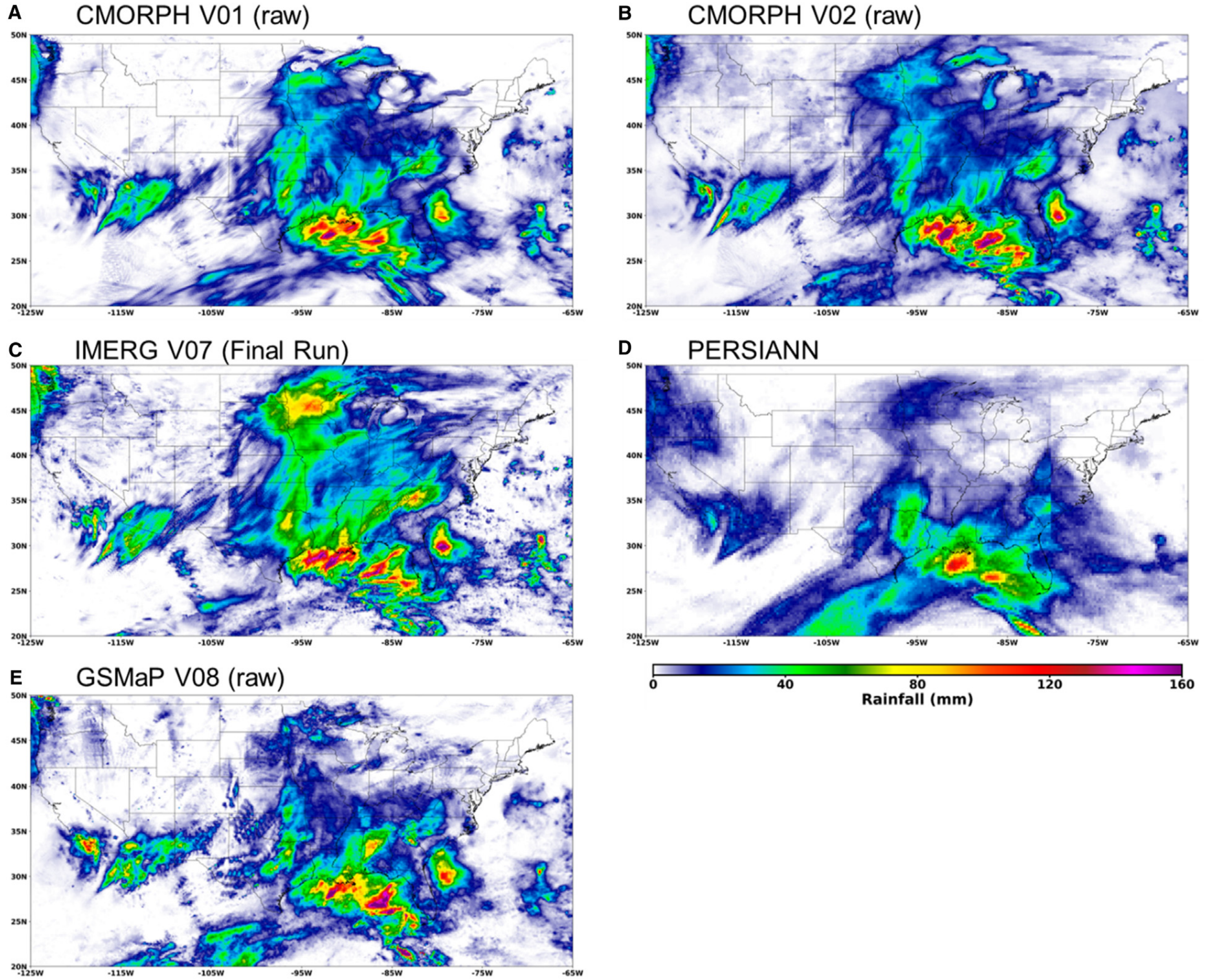

Fig. 12 Accumulated precipitation from 00UTC, December 22, 2023 to 00UTC, December 26, 2023, for four blended satellite precipitation products: (A) CMORPH V01 (raw), (B) CMORPH V02 (raw), (C) IMERG V07 (Final Run), (D) PERSIANN, and (E) GSMaP V08 (raw).

TMPA and IMERG

There are two widely used blended precipitation products that have emerged from NASA's TRMM and GPM programs—The TRMM Multi-Satellite Precipitation Analysis (TMPA; Huffman et al., 2007) and IMERG (Huffman et al., 2023b). Some initial comparisons between the two products can be found in Liu (2016), although the IMERG product continues to evolve during the GPM-era. The latest version IMERG is version 07 (Huffman et al., 2023b). Both TMPA and IMERG exploit GEO IR and LEO PMW data; the former is also adjusted by monthly rain gauges. Like the other blended precipitation products described in this section, these data sets are actually a series of products at various time and space scales, ranging down to 10 km and 30 min.

Conceptually, IMERG was developed to take the "best" attributes of TMPA, CMORPH and PERSIANN to have the best possible blended product. The primary difference between TMPA and IMERG is that IMERG is exploiting PMW algorithms from GPM (Kummerow et al., 2015; Kidd et al., 2016) whereas TMPA relies on algorithms from the TRMM heritage (Kummerow et al., 2001; Ferraro et al., 2005). In addition, IMERG multisatellite precipitation estimates are formally intercalibrated by the highly accurate GMI (Wentz and Draper, 2016). **Fig. 12**C shows the IMERG V07 product for the same event as shown for CMORPH. In this case, IMERG indicates slightly heavier event totals and also a larger areal extent of lighter precipitation. Because GPM was specifically designed to detect falling snow, these lighter precipitation areas in IMERG most likely include snowfall—something that many of the other products have not incorporated in their current operational versions. In addition, the TMPA product has been reprocessed using the observationally based a priori database from GPM such that a uniform precipitation record will be made available starting with TRMM and extending to the lifetime of GPM and even beyond.

PERSIANN

The PERSIANN (Precipitation Estimation from Remotely Sensed Information using Artificial Neural Networks) system uses a neural network function classification/approximation procedures to compute an estimate of rainfall rate at each 0.25 ° × 0.25 ° pixel of the GEO IR measurements (Hsu et al., 1997). An adaptive training feature facilitates updating of the network parameters whenever independent estimates of rainfall are available, including those from PMW and AMW. The PERSIANN system was based on GEO IR and later extended to include the use of both IR and daytime VIS imagery. As is the case for NOAA CMORPH and NASA IMERG, there are several products within PERSIANN that cover various temporal and spatial domains. Most recently, PERSIANN was adopted by NOAA's Climate Data Record (CDR) program as one of its precipitation CDRs (Ashouri et al., 2015; Sadeghi et al., 2021). PERSIANN CDR starts in 1983. **Fig. 12**D is the accumulated precipitation from PERSIANN for the same event as provided for other precipitation products. The same regions of maximum rainfall are indicated, although PERSIANN is underestimating the rainfall peaks compared to other products. In addition, the PERSIANN product is somewhat smoother than the others, likely due to their use of IR only measurements in the retrieval.

GSMAP

Through their involvement with both the TRMM and GPM programs as well as the need to develop precipitation products to support Japan and other Asian nations, Japan's Aerospace Exploration Agency (JAXA), along with other Japanese partners, developed the Global Satellite Mapping of Precipitation (GSMaP) algorithm and suite of products (Kubota et al., 2007; Aonashi et al., 2009). GSMaP is similar in philosophy to NASA's product suite, although the retrieval approach is somewhat different. First, a precipitation detection method is applied (Seto et al., 2005; Kida et al., 2009) to separate the rain/no-rain pixels. The primary difference between the detection methods over land from IMERG and GSMaP is that the rain/no-rain threshold value in JAXA's approach is based on a climatological background whereas that of NASA is more of a static threshold. There are other fundamental differences between the two techniques, however, both exploit the synergistic use of the TRMM/GPM radiometers and radars, and then extend this to all of the PMW "constellation" radiometers. For comparison, **Fig. 12**E shows the GSMaP (version 8) rainfall estimates during the same event as other products described above.

MRMS

In addition to satellite-based multisensor products, ground-based remote sensing methods also utilize blended approaches to achieve improved precipitation estimation over single sensor estimates alone. There are a number of such products available (e.g., Chen and Chandrasekar 2015a; Gou et al., 2020; Cifelli et al., 2024) but for the purposes of this discussion we will focus on MRMS as it is one of the more popular ground-based multisensor precipitation systems and is commonly used in the validation of various satellite QPE and numerical model quantitative precipitation forecasts.

As mentioned in **Ground-Based Radars**, the MRMS system produces a suite of QPE products that covers the conterminous US and some outlying territories (Zhang et al., 2016a). The QPE products include radar-only, gauge adjusted radar, and a multi-sensor product (MSQPE) that utilizes a combination of ground-based radar, rain gauges, satellite estimates, and numerical model forecasts (Martinaitis et al., 2020). All are produced at 1-km resolution. The combination of observations in the MRMS multisensor product generally provides more accurate QPE than the use of radar data alone, especially in areas where radar alone failed to detect precipitation due to significant beam blockage or poor coverage.

Example Applications of Remote Sensing of Precipitation Data

Floods, rainfall-triggered landslides, and droughts are among the most widespread natural hazards on Earth, responsible for tens of thousands of deaths and billions of dollars in property loss. In the U.S. alone, the combination of floods and droughts accounted for over 20% of the annual billion-dollar disaster events between 1980 and 2024 (NOAA, 2024). To forecast and assess these hazards, one generally requires accurate and prompt spatiotemporal information of precipitation. As mentioned, remote sensing techniques including radars and satellites can provide unique ways to observe the spatial distribution of precipitation at various scales. In the United States and a few other countries, ground radar based QPE systems are primary tools for real-time precipitation monitoring. However, in many countries around the world, especially less-developed countries, satellite-based precipitation estimation may be the best and only source of rainfall data due to a lack of surface observing networks (Adler et al., 2003). Naturally, the satellite precipitation data is of potential use for monitoring flood, landslide and drought hazards over such data sparse areas.

Flood Monitoring and Prediction

Precipitation is required information for real-time forecasting of floods. A typical flood forecasting model system is usually based on one or more hydrological models. These models can convert rainfall processes into land surface hydrological processes. The model system can be as simple as a flood guidance index, which is defined as the amount of rain required over a given time and area to produce bank-full conditions on small streams (Clark et al., 2014) and can be calculated using simple hydrological formulas and/or hydrological models (Smith, 2003). For example, the National Weather Service (NWS) traditionally use flash flood guidance (FFG) products based on radar-sensed precipitation products for forecasting flash floods (Clark et al., 2014). The NWS forecasters rely primarily on basin-specific FFG products displayed within the flash flood monitoring and prediction system (FFMP) to provide warnings of impending flash floods.

To better represent the underlying hydrological fluxes and storages in a more physical way, a sophisticated distributed hydrological model is usually needed. One example is the NOAA National Water Model (NWM) that simulates observed and forecast streamflow over the entire continental United States (CONUS), southern Alaska (Cook Inlet, Copper River Basin, and Prince William Sound regions), Hawaii, Puerto Rico and the US Virgin Islands (Cosgrove, 2016; Frame et al., 2021). The backbone of the NWM is WRF-Hydro (Gochis et al., 2015), which is a parallelized distributed hydrologic model that can either be forced offline using prescribed atmospheric forcing variables, or coupled to the Advanced Research version of the WRF (WRF-ARW) atmospheric model (Skamarock et al., 2008). In addition to the NWM, NOAA forecasters also use other physically-based hydrologic modeling systems, such as the Flooded Locations and Simulated Hydrographs (FLASH; Gourley et al., 2017). Ground-radar based MRMS precipitation estimates are the key driver of both the NWM and FLASH for flood monitoring and prediction. In addition, NASA, in partnership of University of Maryland, has developed a Global Flood Monitoring System by coupling the Variable Infiltration Capacity (VIC) model with a runoff-routing model and using satellite remote sensing of precipitation products as inputs (Wu et al., 2014).

Landslide and Debris Flow Forecasting

High-intensity rainfall processes caused by intense storms have great potential to trigger rapidly moving landslides and/or debris flows, resulting in casualties and property damage across the world, especially in areas of complex terrain. Spatiotemporal precipitation data gained from remote sensing make it possible to conduct global-scale landslide hazard assessment.

Like flood forecasting, predicting rainfall-triggered landslides usually requires the rainfall rates and their history and a model that, ideally, simulates the important watershed characteristics such as vegetation, soil properties, and terrain slope. The watershed characteristics are especially important for anticipating post wildfire impacts where, depending on when the area was burned, may be susceptible to landslides/debris flows for even short duration precipitation events (Oakley et al., 2023; Gourley et al., 2020).

One simple approach to map landslide susceptibility is to use satellite remote sensing, including remote sensing of precipitation, and geographic information system (GIS) techniques using a GIS-based weighted linear combination method (Hong et al., 2007a) and an adjusted empirical relationship between rainfall intensity-duration and landslide occurrence (Hong et al., 2007b). Kirschbaum et al. (2009) further improved this landslide susceptibility algorithm by introducing a stochastic method to forecast potential landslides using global remote sensing precipitation products. A more sophisticated approach is to use process-based landslide models to compute the stability of slope. There are many landslide models that potentially can be used for landslide forecasting, e.g., Transient Rainfall Infiltration and Grid-based Regional Slope-stability (TRIGRS; Baum et al., 2008, 2010) and High Resolution Slope Stability Simulator HIRESSS (Rossi et al., 2013). Recently, researchers have started to couple the landslide models with distributed hydrological models to better represent the physical processes that cause both landslide and flood hazards (Ebel et al., 2023). For example, Zhang et al. (2016b) developed the iCRESTRIGRS model by integrating a hydrological model with the TRIGRS landslide model, which has been successfully applied to forecast rainfall-triggered landslides in North Carolina using remotely sensing precipitation data as input.

Probable Maximum Precipitation and Precipitation Frequency Estimation

Probable Maximum Precipitation (PMP and Precipitation Frequency (PF) both provide estimates of extreme precipitation; however, they are not the same quantity and are aimed for different applications. PF is the probability (in a given year) of observing a precipitation event of a defined depth and duration at a particular location (e.g., 10% chance of observing 6 inches of rain over 3 hours). PF estimates are disseminated by the NOAA Atlas 14 product and its future evolution, NOAA Atlas 15 (https://www.weather.gov/owp/hdsc), which will be informed by climate variability.

Planning, design, and management of infrastructure including culverts, bridges, detention ponds, and sewers has long relied on extreme rainfall statistics, such as the "100-year storm" and the so-called rainfall Intensity-Duration-Frequency (IDF) curves. In the US, these statistics are commonly disseminated by the NOAA Atlas 14 PF product (Perica et al., 2015), which is derived from historical rain gauge records that typically span several decades. However, the Atlas 14 product does not include data after 2012, and the data record used in the early volumes of Atlas 14 was even shorter. While this product is currently the most reliable and widely used design guidance of IDF statistics, there are growing concerns about this method's uncertainty and inability. For example, the most recent heavy rainfall events in a given region are not incorporated. The changing frequency and spatiotemporal patterns of heavy rainfall events due to climate change are not taken into consideration. These may leave infrastructure "underdesigned" in the face of current and future heavy rainfall events.

In contrast to PF, PMP represents the greatest depth of precipitation meteorologically possible for a given duration and design watershed, or a given storm area at a particular location, at a particular time of year (World Meteorological Organization). PMP is commonly used to establish design criteria for high-risk infrastructure such as dams and nuclear power plants. Similar to the PF Atlas 14 methodology, almost all statistical PMP estimates are traditionally based on gauge records.

Recent advances in remote sensing of precipitation and long-term remote sensing precipitation products offer unprecedent opportunities to depict the space-time structure of heavy rainfall at a high level of detail that cannot be addressed by gauge information alone. Methods such as stochastic storm transposition (SST; Wright et al., 2013, 2020) have been demonstrated to be efficient alternatives to derive rainfall IDF estimates. SST is distinct from Atlas 14's method as it relies on spatially complete rainfall estimates, rather than long records of rain gage observations at one or several specific locations. In the context of SST or similar approaches, the remote sensing precipitation datasets described in this chapter (20+ years of record) can sufficiently support the estimates of "full-range" IDF statistics from 2-year to 1000-year return periods. The remote sensing precipitation datasets will also bring new opportunities for PMP estimation (e.g., Yang et al., 2018) and for deriving long-term, high-resolution "storm catalog", especially over sparsely gauged or ungauged areas.

Drought Forecasting and Evaluation

Drought is an insidious natural hazard that can cause tremendous loss to agriculture, ecosystems, and other sectors. Reliable drought monitoring and early warning are important for drought preparedness planning and mitigation to reduce potential impacts, especially for early famine warnings (e.g., Funk, 2019). Traditionally, drought monitoring is usually based on drought indices. Some of these well-known indices that use precipitation as input include Standardized Precipitation Index (SPI) and Palmer Drought Severity Index (PDSI) (Palmer, 1965) among others. These drought indices have their own advantages and limitations due to the multifaceted nature of drought: meteorological drought, hydrological drought, agricultural drought, and socioeconomic (Wilhite, 2005). Therefore, combining or utilizing multiple indices can achieve better results. For example, the US Drought Monitor (USDM) classifies drought conditions into different drought categories to provide composite drought information by integrating multiple drought indices. The integrated indices have been widely used to help decision-making at local to state levels. In a recent study, Hao et al. (2016) applied an ordinal regression model to characterize droughts in USDM drought categories based on several drought indices, in which the probability of each drought category can be estimated. By taking advantage of real-time precipitation, vegetation, and soil moisture data from remote sensing (e.g., AghaKouchak et al., 2015), these drought assessment and quantification methods can provide prompt estimation of the severity of droughts to assist decision makers in taking timely and appropriate action in order to save millions of lives in drought-affected areas.

Summary

Remote sensing techniques, including radars and satellites, are powerful in monitoring precipitation and atmospheric conditions at good spatial and temporal resolutions. Over the past few decades, tremendous technological advancement has been made in quantitative remote sensing of precipitation, and numerous approaches have been developed to retrieve precipitation using various remote sensing observations. Each approach has its own advantages that are dictated by the particular needs for the information. In general, radars and/or the IR methods are used for short-term, high-spatial resolution applications such as flash flood prediction. At global or climate scales, the PMW-based retrievals are usually preferred. In this regard, no single approach can be defined as the best one, although in terms of instantaneous precipitation retrieval accuracy, it is generally accepted that the active MW methods (i.e., radars) are the most accurate, followed by PMW approaches over ocean, PMW approaches over land, IR and VIS methods.

In addition, the ground-based radars have been used for precipitation observations for many decades, while the space-based sensors were not necessarily designed for rainfall retrieval but more for tracking cloud features and monitoring atmospheric temperature and moisture. As was described, current and near-term missions are being designed specifically for precipitation monitoring and include AMW sensors (e.g., GPM mission, EarthCARE mission, and Atmosphere Observing System mission). The current status of precipitation products now tends to focus on blended techniques which have proven to yield the most accurate results. As we move into the second quarter of this century and an AI era, more advances are anticipated through new sensors such as CubeSats or small satellites or multifrequency active/passive systems, through incorporating modern AI approaches and improvements in estimating precipitation, especially light rain and falling snow over complex terrain regions. These advancements are sure to lead to additional scientific insight into precipitation systems, to provide improved data for societal applications, and to better inform NWP and climate models.

Disclaimer

This chapter is dedicated to former GPM Project Scientist Gail Skofronick-Jackson (1963–2021). Some parts of this chapter were adopted from the first edition written by R.R. Ferraro, G. Skofronick-Jackson, Y. Hong, and K. Zhang. Scientific results and conclusions as well as any views and opinions expressed herein are those of the author(s) and do not necessarily reflect the views of NOAA or the Department of Commerce.

References

Adler, R.F., Negri, A.J., 1988. A satellite infrared technique to estimate tropical convective and stratiform rainfall. J. Appl. Meteorol. 27, 30–51.

Adler, R.F., Kidd, C., Petty, G., Morrissey, M., Goodman, H.M., 2001. Intercomparison of global precipitation products: the third precipitation intercomparison project (PIP-3). Bull. Am. Meteorol. Soc. 82, 1377–1396.

Adler, R.F., Huffman, G.J., Chang, A., Ferraro, R., Xie, P., Janowiak, J., Rudolf, B., Schneider, U., Curtis, S., Bolvin, D., Gruber, A., Susskind, J., Arkin, P., Nelkin, E., 2003. The version-2 Global Precipitation Climatology Project (GPCP) monthly precipitation analysis (1979–present). J. Hydrometeorol. 4, 1147–1167.

Adler, R.F., Wang, J.-J., Gu, G., Huffman, G.J., 2009. A ten-year tropical rainfall climatology based on a composite of TRMM products. J. Meteorol. Soc. Jpn. Ser. II. 87A, 281–293.

Adler, R.F., et al., 2018. The global precipitation climatology project (GPCP) monthly analysis (new version 2.3) and a review of 2017 global precipitation. Atmosphere 9, 138.

AghaKouchak, A., Farahmand, A., Melton, F.S., Teixeira, J., Anderson, M.C., Wardlow, B.D., Hain, C.R., 2015. Remote sensing of drought: progress, challenges and opportunities. Rev. Geophys. 53, 452–480. https://doi.org/10.1002/2014RG000456.

Aonashi, K., et al., 2009. GSMAP passive microwave precipitation retrieval algorithm: algorithm description and validation. J. Meteorol. Soc. Jpn. 87, 119–136.

Arkin, P.A., 1979. The relationship between fractional coverage of high cloud and rainfall accumulations during GATE over the B-scale array. Mon. Weather Rev. 106, 1153–1171.

Arkin, P.A., Meisner, B.N., 1987. The relationship between large-scale convective rainfall and cold cloud over the Western Hemisphere during 1982–84. Mon. Weather Rev. 115, 51–74.

Arkin, P.A., Janowiak, J., 1991. Analysis of the global distribution of precipitation. Dynam. Atmos. Oceans 16, 5–16.

Arkin, P.A., Xie, P.P., 1994. The global precipitation climatology project: first Algorithm Intercomparison Project. Bull. Am. Meteorol. Soc. 75, 401–419.

Ashouri, H., et al., 2015. PERSIANN-CDR: daily precipitation climate data record from multisatellite observations for hydrological and climate studies. Bull. Am. Meteorol. Soc. 96, 69–84.

Ba, M.B., Gruber, A., 2001. GOES multispectral rainfall algorithm (GMSRA). J. Appl. Meteorol. 40, 1500–1514.

Barrett, E.C., Martin, D.W., 1981. The Use of Satellite Data in Rainfall Monitoring. Academic Press, London.

Barrett, E.C., Dodge, J., Goodman, H.M., Janowiak, J., Kidd, C., Smith, E.A., 1994. The first WetNet precipitation intercomparison project. Rem. Sens. Rev. 11, 49–60.

Baum, R.L., Savage, W.Z., Godt, J.W., 2008. TRIGRS—A Fortran Program for Transient Rainfall Infiltration and Grid-Based Regional Slope-Stability Analysis, Version 2.0. U.S. Geological Survey Open-File Report, 2008-1159, 75 pp.

Baum, R.L., Godt, J.W., Savage, W.Z., 2010. Estimating the timing and location of shallow rainfall-induced landslides using a model for transient, unsaturated infiltration. J. Geophys. Res. 115 (F03013), 1–26.

Behrangi, A., Song, Y., 2020. A new estimate for oceanic precipitation amount and distribution using complementary precipitation observations from space and comparison with GPCP. Environ. Res. Lett. 15 (12), 124042.

Bellerby, T., 2004. A feature-based approach to satellite precipitation monitoring using geostationary IR imagery. J. Hydrometeorol. 5, 910–921.

Bellerby, T., 2006. High-resolution 2-D cloud-top advection from geostationary satellite imagery. IEEE Trans. Geosci. Rem. Sens. 44, 3639–3648.

Bellon, A., Lovejoy, S., Austin, G.L., 1980. Combining satellite and radar data for the shortrange forecasting of precipitation. Mon. Weather Rev. 108, 1554–1556.

Bringi, V.N., Chandrasekar, V., 2001. Polarimetric Doppler Weather Radar: Principles and Applications. Cambridge University Press, p. 664.

Boukabara, S., Garrett, K., Grassotti, C., Iturbide-Sanchez, F., Chen, W., Jiang, Z., Clough, S.A., Zhan, X., Liang, P., Liu, Q., Islam, T., Zubko, V., Mims, A., 2013. A physical approach for a simultaneous retrieval of sounding, surface, hydrometeor, and cryospheric parameters from SNPP/ATMS. J. Geophys. Res. Atmos. 118, 12600–12619.

Boukabara, S., Garrett, K., Chen, W., Iturbide-Sanchez, F., Grassotti, C., Kongoli, C., Chen, R., Liu, Q., Yan, B., Weng, F., Ferraro, R., Kleespies, T., Meng, H., 2011. MiRS: an all-weather satellite data assimilation and retrieval system. IEEE Trans. Geosci. Rem. Sens. 49, 3249–3272.

Bytheway, J.L., Thompson, E.J., Yang, J., Chen, H., 2023. Evaluating satellite precipitation estimates over oceans using passive aquatic listeners. Geophys. Res. Lett. 50, e2022GL102087.

Cattani, E., Torricella, F., Laviola, S., Levizzani, V., 2009. On the statistical relationship between cloud optical and microphysical characteristics and rainfall intensity for convective storms over the Mediterranean. Nat. Hazards Earth Syst. Sci. 9, 2135–2142.

Chandrasekar, V., Chen, H., Philips, B.J., 2018. Principles of high-resolution radar network for hazard mitigation and disaster management in an urban environment. J. Meteor. Soc. Japan 96A, 119–139.

Chen, H., Chandrasekar, V., 2015a. The quantitative precipitation estimation system for Dallas-Fort Worth (DFW) urban remote sensing network. J. Hydrol. 531 (2), 259–271.

Chen, H., Chandrasekar, V., 2015b. Estimation of light rainfall using ku-band dual-polarization radar. IEEE Trans. Geosci. Rem. Sens. 53 (9), 5197–5208. https://doi.org/10.1109/TGRS.2015.2419212.

Chen, H., Chandrasekar, V., Bechini, R., 2017. An improved dual-polarization radar rainfall algorithm (DROPS2.0): application in NASA IFloodS field campaign. J. Hydrometeorol. 18, 917–937.

Chen, H., Chandrasekar, V., 2018. Real-time wind velocity retrieval in the precipitation system using high-resolution operational multi-radar network. In: Remote Sensing of Aerosols, Clouds, and Precipitation, pp. 315–339. Elsevier.

Chen, H., Chandrasekar, V., Tan, H., Cifelli, R., 2019. Rainfall estimation from ground radar and TRMM precipitation radar using hybrid deep neural networks. Geophys. Res. Lett. 46, 10669–10678.

Chen, H., Chandrasekar, V., Cifelli, R., Xie, P., 2020. A machine learning system for precipitation estimation using satellite and ground radar network observations. IEEE Trans. Geosci. Rem. Sens. 58 (2), 982—994.

Chen, R., Chang, F., Li, Z., Ferraro, R., Weng, F., 2008. Impact of the vertical variation of cloud droplet size on the estimation of cloud liquid water path and rain detection. J. Atmos. Sci. 64, 3843—3853.

Cifelli, R., Chandrasekar, V., Lim, S., Kennedy, P.C., Wang, Y., Rutledge, S.A., 2011. A new dual-polarization radar rainfall algorithm: application in Colorado precipitation events. J. Atmos. Ocean. Technol. 28, 352—364.

Cifelli, R., et al., 2024. Advanced quantitative precipitation information: improving monitoring and forecasts of precipitation, streamflow, and coastal flooding in the San Francisco Bay area. Bull. Am. Meteorol. Soc. 105, E313—E331.

Cifelli, R., Chandrasekar, V., Chen, H., Johnson, L.E., 2018. High resolution radar quantitative precipitation estimation in the San Francisco Bay Area: rainfall monitoring for the urban environment. J. Meteor. Soc. Japan 96A, 141—155.

Clark, R.A., Gourley, J.J., Flamig, Z.L., Hong, Y., Clark, E., 2014. CONUS — wide evaluation of national weather service flash flood guidance products. Weather Forecast. 29, 377—392.

Cosgrove, B.D., 2016. Hydrologic modeling at the national water center: operational implementation of the WRF-Hydro model to support National Weather Service Hydrology. In: 30th Conf. On Hydrology. Amer. Meteor. Soc., New Orleans, LA, 4.2. https://ams.confex.com/ams/96Annual/webprogram/Paper283089.html.

Derin, Y., Anagnostou, E., Berne, A., Borga, M., Boudevillain, B., Buytaert, W., Chang, C.-H., Chen, H., Delrieu, G., Hsu, Y.C., et al., 2019. Evaluation of GPM-era global satellite precipitation products over multiple complex terrain regions. Rem. Sens. 11, 2936.

Dodge, J., Goodman, H.M., 1994. The WetNet project. Rem. Sens. Rev. 11, 5—21.

Ebel, B.A., Shephard, Z.M., Walvoord, M.A., Murphy, S.F., Partridge, T.F., Perkins, K.S., 2023. Modeling post-wildfire hydrologic response: review and future directions for applications of physically based distributed simulation. Earth's Future 11, e2022EF003038. https://doi.org/10.1029/2022EF003038.

Ebert, E.E., Manton, M.J., Arkin, P.A., Allam, R.J., Holpin, C.E., Gruber, A., 1996. Results from the GPCP algorithm intercomparison programme. Bull. Am. Meteorol. Soc. 77, 2875—2887.

Ebert, E.E., Manton, M.J., 1998. Performance of satellite rainfall estimation algorithms during TOGA COARE. J. Atmos. Sci. 55, 1537—1557.

Ebert, E.E., Janowiak, J.E., Kidd, C., 2007. Comparison of near-real-time precipitation estimates from satellite observations and numerical models. Bull. Am. Meteorol. Soc. 88, 47—64.

Ehsani, M.R., Behrangi, A., Adhikari, A., Song, Y., Huffman, G.J., Adler, R.F., Bolvin, D.T., Nelkin, E.J., 2021. Assessment of the advanced very high resolution radiometer (AVHRR) for snowfall retrieval in high latitudes using CloudSat and machine learning. J. Hydrometeorol. 22, 1591—1608.

Fan, J., Wang, Y., Rosenfeld, D., Liu, X., 2016. Review of aerosol-cloud interactions: mechanisms, significance and challenges. J. Atmos. Sci. 73, 4221—4252.

Ferraro, R.R., Marks, G.F., 1995. The development of SSM/I rain-rate retrieval algorithms using ground-based radar measurements. J. Atmos. Ocean. Technol. 12, 755—770.

Ferraro, R.R., Grody, N.C., Marks, G.F., 1994. Effects of surface conditions on rain identification using the SSM/I. Rem. Sens. Rev. 11, 195—209.

Ferraro, R.R., 1997. Special sensor microwave imager derived global rainfall estimates for climatological applications. J. Geophys. Res. 102, 16715—16735.

Ferraro, R.R., Weng, F., Grody, N., Zhao, L., Meng, H., Kongoli, C., Pellegrino, P., Qiu, S., Dean, C., 2005. NOAA operational hydrological products derived from the AMSU. IEEE Trans. Geosci. Rem. Sens. 43, 1036—1049.

Ferraro, R.R., et al., 2013. An evaluation of microwave land surface emissivities over the continental United States to benefit GPM-era Precipitation Algorithms. IEEE Trans. Geosci. Rem. Sens. 51, 378—398.

Frame, J.M., Kratzert, F., Raney II, A., Rahman, M., Salas, F.R., Nearing, G.S., 2021. Post-post-processing the national water model with long short-term memory networks for streamflow predictions and model diagnostics. J. Am. Water Resour. Assoc. 57 (6), 885—905.

Fujita, M., Satake, M., 1997. Rainfall rate profiling with attenuation-frequency radar using nonlinear LMS technique under a constraint on path-integrated rainfall rate. Int. J. Rem. Sens. 18, 1137—1147.

Funk, C., 2019. Recognizing the famine early warning systems network: over 30 years of drought early warning science advances and partnerships promoting global food security. Bull. Am. Meteorol. Soc. 100, 1011—1027.

Gasiewski, A.J., 1993. Microwave radiative transfer in hydrometeors. In: Janssen, M.A. (Ed.), Atmospheric Remote Sensing by Microwave Radiometry. John Wiley, New York, pp. 91—144.

Giangrande, S.E., Ryzhkov, A.V., 2008. Estimation of rainfall based on the results of polarimetric echo classification. J. Appl. Meteorol. Climatol. 47, 2445—2462.

Gochis, D.J., Yu, W., Yates, D.N., 2015. The WRF-Hydro Model Technical Description and User's Guide, Version 1.0. NCAR Tech. Doc., 120 pp. https://www.ral.ucar.edu/projects/wrf_hydro.

Gopolan, K., Wang, N.Y., Liu, C., Ferraro, R., 2010. Version 7 of the TRMM 2A12 land precipitation algorithm. J. Appl. Meteorol. Climatol. 27, 1343—1354.

Gou, Y., Chen, H., Chandrasekar, V., 2020. A dynamic approach to quantitative precipitation estimation using multiradar multigauge network. IEEE Trans. Geosci. Rem. Sens. 58 (9), 6376—6390. https://doi.org/10.1109/TGRS.2020.2976724.

Gourley, J.J., Flamig, Z.L., Vergara, H., Kirstetter, P.E., Clark III, R.A., Argyle, E., Arthur, A., Martinaitis, S., Terti, G., Erlingis, J.M., Hong, Y., Howard, K.W., 2017. The FLASH project: improving the tools for flash flood monitoring and prediction across the United States. Bull. Am. Meteorol. Soc. 98, 361—372. https://doi.org/10.1175/BAMS-D-15-00247.1.

Gourley, J.J., Vergara, H., Arthur, A., Clark III, R.A., Staley, D., Fulton, J., Hempel, L., Goodrich, D.C., Rowden, K., Robichaud, P.R., 2020. Predicting the floods that follow the flames. Bull. Am. Meteorol. Soc. 101, E1101—E1106. https://doi.org/10.1175/BAMS-D-20-0040.1.

Griffith, C.G., Woodley, W.L., Grube, P., Martin, D.W., Stout, J., Sikdar, D.N., 1978. Rain estimation from geosynchronous satellite imagery — visible and infrared studies. Mon. Weather Rev. 106, 1153—1171.

Grody, N.C., 1991. Classification of snow cover and precipitation using the Special Sensor Microwave/imager (SSM/I). J. Geophys. Res. 96, 7423—7435.

Hao, Z.C., Hong, Y., Xia, Y.L., Singh, V.P., Hao, F.H., Cheng, H.G., 2016. Probabilistic drought characterization in the categorical form using ordinal regression. J. Hydrol. 535, 331—339.

Haynes, J.M., Stephens, G., 2007. Tropical oceanic cloudiness and incidence of precipitation: early results from CloudSat. Geophys. Res. Lett. 34 (L09811), 1—5.

Hitschfeld, W., Bordan, J., 1954. Errors inherent in the radar measurement of rainfall at attenuating wavelengths. J. Meteorol. 11, 58—67.

Hong, Y., Adler, R., Huffman, G., 2007a. Use of satellite remote sensing data in the mapping of global landslide susceptibility. Nat. Hazards 43, 245—256.

Hong, Y., Adler, R., Huffman, G., 2007b. An experimental global prediction system for rainfall-triggered landslides using satellite remote sensing and geospatial datasets. IEEE Trans. Geosci. Rem. Sens. 45, 1671—1680.

Hong, Y., Liu, G., 2015. The characteristics of ice cloud properties derived from CloudSat and CALIPSO measurements. J. Clim. 28, 3880—3901.

Hou, A.Y., et al., 2014. The global precipitation measurement mission. Bull. Am. Meteorol. Soc. 95, 701—722.

Hsu, K., Gao, X., Sorooshian, S., Gupta, H.V., 1997. Precipitation estimation from remotely sensed information using artificial neural networks. J. Appl. Meteorol. 36, 1176—1190.

Huffman, G.J., Adler, R.F., Arkin, P.A., Chang, A., Ferraro, R., Gruber, A., Janowiak, J., McNab, A., Rudolf, B., Schneider, U., 1997. The global precipitation climatology project (GPCP) combined precipitation dataset. Bull. Am. Meteorol. Soc. 78, 5—20.

Huffman, G.J., Adler, R.F., Morrissey, M.M., Bolvin, D.T., Curtis, S., Joyce, R., McGavock, B., Susskind, J., 2001. Global precipitation at one-degree daily resolution from multisatellite observations. J. Hydrometeorol. 2, 36—50.

Huffman, G.J., Adler, R.F., Bolvin, D.T., Gu, G., Nelkin, E.J., Bowman, K.P., Hong, Y., Stocker, E., Wolff, D., 2007. The TRMM multisatellite precipitation analysis (TMPA): quasi-global, multiyear. combined-sensor precipitation estimates at fine scales. J. Hydrometeorol. 8, 38—55.

Huffman, G.J., Adler, R.F., Behrangi, A., Bolvin, D.T., Nelkin, E.J., Gu, G., Ehsani, M.R., 2023a. The new version 3.2 global precipitation climatology project (GPCP) monthly and daily precipitation products. J. Clim. 36, 7635—7655.

Huffman, G.J., Bolvin, D.T., Joyce, R., Nelkin, E.J., Tan, J., Braithwaite, D., Hsu, K., Kelley, O.A., Nguyen, P., Sorooshian, S., Watters, D.C., West, B.J., Xie, P., 2023b. NASA Global Precipitation Measurement (GPM) Integrated Multi-satellitE Retrievals for GPM (IMERG) Version 07. NASA/GSFC [online] Available https://gpm.nasa.gov/sites/default/files/2023-07/IMERG_V07_ATBD_final_230712.pdf.

Huffman, G.J., Adler, R.F., Bolvin, D.T., Gu, G., 2009. Improving the global precipitation record: GPCP Version 2.1. Geophys. Res. Lett. 36, 1—17. L17808.

Iguchi, T., Meneghini, R., 1994. Intercomparison of single frequency methods for receiving a vertical rain profile from airborne and spaceborne radar data. J. Atmos. Ocean. Technol. 11, 1507—1516.

Iguchi, T., Kozu, T., Meneghini, R., Awaka, J., Okamoto, K., 2000. Rain-profiling algorithm for the TRMM precipitation radar. J. Appl. Meteorol. 39, 2038—2052.

Iguchi, T., Oki, R., Smith, E.A., Furuhama, Y., 2002. Global Precipitation Measurement program and the development of dual-frequency precipitation radar. J. Commun. Res. Lab. 49, 37—45.

Iguchi, T., Kozu, T., Kwiatkowski, J., Meneghini, R., Awaka, J., Okamoto, K., 2009. Uncertainties in the rain profiling algorithm for the TRMM precipitation radar. J. Meteorol. Soc. Jpn. 87A, 1—30.

Janowiak, J., Xie, P., 1999. CAMS—OPI: a global satellite—rain gauge merged product for real-time precipitation monitoring applications. J. Clim. 12, 3335—3342.

Joyce, R.J., Janowiak, J.E., Arkin, P.A., Xie, P., 2004. CMORPH: a method that produces global precipitation estimates from passive microwave and infrared data at high spatial and temporal resolution. J. Hydrometeorol. 5, 487—503.

Kida, S., Shige, S., Kubota, T., Aonashi, K., Okamoto, K., 2009. Improvement of rain/no-rain classification methods for microwave radiometer observations over the ocean using a 37 GHz emission signature. J. Meteorol. Soc. Jpn. 87, 165—181.

Kidd, C., Becker, A., Huffman, G.J., Muller, C.L., Joe, P., Skofronick-Jackson, G., Kirschbaum, D.B., 2017. So, how much of the earth's surface is covered by rain gauges? Bull. Am. Meteorol. Soc. 98, 69—78.

Kidd, C., Huffman, G., Maggioni, V., Chambon, P., Oki, R., 2021. The global satellite precipitation constellation: current status and future requirements. Bull. Am. Meteorol. Soc. 102, E1844—E1861.

Kidd, C., Ferraro, R.R., Levizzani, V., 2010. The international precipitation working Group. Bull. Am. Meteorol. Soc. 8, 1095—1099.

Kidd, C., Matsui, T., Chern, J., Mohr, K., Kummerow, C., Randel, D., 2016. Global precipitation estimates from cross-track passive microwave observations using a physically based retrieval scheme. J. Hydrometeorol. 17, 383—400.

Kidder, S.Q., Vonder Haar, T.H., 1995. Satellite Meteorology: An Introduction. Academic Press, New York.

Kirschbaum, D.B., Adler, R., Hong, Y., Lerner-Lam, A., 2009. Evaluation of a preliminary satellite-based landslide hazard algorithm using global landslide inventories. Nat. Hazards Earth Syst. Sci. 9, 673—686.

Kniveton, D.R., Motta, B.C., Goodman, H.M., Smith, M., LaFontaine, F.J., 1994. The first WetNet precipitation intercomparison project: generation of results. Rem. Sens. Rev. 11, 243—302.

Kongoli, C., Meng, H., Dong, J., Ferraro, R., Wang, N.-Y., 2015. A snowfall detection algorithm over land utilizing high-frequency passive microwave measurements — application to ATMS. J. Geophys. Res. 120, 1918—1932.

Kubota, T., et al., 2007. Global precipitation map using satellite-borne microwave radiometers by the GSMAP project: production and validation. IEEE Trans. Geosci. Rem. Sens. 45, 2259—2275.

Kuligowski, R.J., 2002. A self-calibrating real-time GOES rainfall algorithm for short-term rainfall estimates. J. Hydrometeorol. 3, 112—130.

Kuligowski, R.J., Li, Y., Zhang, Y., 2013. Impact of TRMM data on a low-latency, high-resolution precipitation algorithm for flash-flood forecasting. J. Appl. Meteorol. Climatol. 52, 1379—1393.

Kuligowski, R.J., Li, Y., Hao, Y., Zhang, Y., 2016. Improvements to the GOES-R rainfall rate algorithm. J. Hydrometeorol. 17, 1693—1704.

Kummerow, C., Olson, W.S., Giglio, L., 1996. A simplified scheme for obtaining precipitation and vertical hydrometeor profile from passive microwave. IEEE Trans. Geosci. Rem. Sens. 34, 1213—1232.

Kummerow, C., Barnes, W., Kozu, T., Shiue, J., Simpson, J., 1998. The tropical rainfall measuring mission (TRMM) sensor package. J. Atmos. Ocean. Technol. 15, 809—817.

Kummerow, C., Hong, Y., Olson, W.S., Yang, S., Adler, R.F., McCollum, J., Ferraro, R., Petty, G., Shin, D., Wilheit, T.T., 2001. The evolution of the Goddard profiling algorithm (GPROF) for rainfall estimation from passive microwave sensors. J. Appl. Meteorol. 40, 1801—1819.

Kummerow, C., Randel, D., Kulie, M., Wang, N.-Y., Ferraro, R., Munchak, S.J., Petkovic, V., 2015. The evolution of the Goddard profiling algorithm to a fully parametric scheme. J. Atmos. Ocean. Technol. 32, 2265—2280.

Kuo, K.-S., Smith, E.A., Haddad, S., Im, E., Iguchi, T., Mugnai, A., 2004. Mathematical physical framework for retrieval of rain DSD properties from dual-frequency Ku/Ka-band satellite radar. J. Atmos. Sci. 61, 2349—2369.

Laviola, S., Levizzani, V., 2011. The 183-WSL fast rain rate retrieval algorithm. Part I: retrieval design. Atmos. Res. 99, 443—461.

Laviola, S., Levizzani, V., Cattani, E., Kidd, C., 2013. The 183-WSL fast rain rate retrieval algorithm. Part II: validation using ground radar measurements. Atmos. Res. 134, 77—86.

L'Ecuyer, T.S., Stephens, G.L., 2002. An estimation-based precipitationretrieval algorithm for attenuating radars. J. Appl. Meteorol. 41, 272—285.

Li, W., Chen, H., Han, L., 2023. Polarimetric radar quantitative precipitation estimation using deep convolutional neural networks. IEEE Trans. Geosci. Rem. Sens. 61, 1—11, 4102911.

Li, W., Chen, H., Han, L., 2024a. Improving explainability of deep learning for polarimetric radar rainfall estimation. Geophys. Res. Lett. 51, e2023GL107898.

Li, W., Chen, H., Han, L., Lee, W.C., 2024b. StarNet: a deep learning model for enhancing polarimetric radar quantitative precipitation estimation. IEEE Transactions on Geoscience and Remote Sensing 62, 1—13, 4106513. In this issue. https://doi.org/10.1109/TGRS.2024.3426532.

Liu, G., 2008. Deriving snow cloud characteristics from CloudSat observations. J. Geophys. Res. Atmos. 113 (D8).

Liu, S., et al., 2020. The NOAA microwave integrated retrieval system (MiRS): validation of precipitation from multiple polar-orbiting satellites. In: IEEE Journal of Selected Topics in Applied Earth Observations and Remote Sensing, vol. 13, pp. 3019—3031. https://doi.org/10.1109/JSTARS.2020.3000348.

Liu, S., Grassotti, C., Liu, Q., 2023. Use of a U-net architecture to improve microwave integrated retrieval system (MiRS) precipitation rates. In: IEEE Transactions on Geoscience and Remote Sensing, vol. 61, pp. 1—11, 4105611. https://doi.org/10.1109/TGRS.2023.3315212.

Liu, Z., 2016. Comparison of integrated multisatellite retreivals for GPM (IMERG) and TRMM multisatellite precipitation analysis (TMPA) monthly precipitation products: initial results. J. Hydrometeorol. 17, 777—790.

Lovejoy, S., Austin, G.L., 1979. The delineation of rain areas from visible and IR satellite data from GATE and mid-latitudes. Atmos.-Ocean 17, 77—92.

Maggioni, V., Meyers, P., Robinson, M., 2016. A review of high-resolution satellite precipitation product accuracy during the tropical rainfall measuring mission (TRMM) era. J. Hydrometeorol. 17, 1101—1117.

Martinaitis, S.M., Osborne, A.P., Simpson, M.J., Zhang, J., Howard, K.W., Cocks, S.B., Arthur, A., Langston, C., Kaney, B.T., 2020. A physically based multisensor quantitative precipitation estimation approach for gap-filling radar coverage. J. Hydrometeorol. 21, 1485—1511. https://doi.org/10.1175/JHM-D-19-0264.1.

Matrosov, S.Y., 2007. Potential for attenuation-based estimations of rainfall rate from CloudSat. Geophys. Res. Lett. 34, L05817. https://doi.org/10.1029/2006GL029161.

McCollum, J.R., Ferraro, R.R., 2003. The next generation of NOAA/NESDIS SSM/I, TMI and AMSR-E microwave land rainfall algorithms. J. Geophys. Res. 108, 8382—8404.

Meneghini, R., Nakamura, K., Ulbrich, C.W., Atlas, D., 1989. Experimental tests of methods for the measurement of rainfall rate using an airborne dual-wavelength radar. J. Atmos. Ocean. Technol. 6, 637—651.

Meneghini, R., Kozu, T., 1990. Spaceborne Weather Radar. Artech House, Norwood, MA.

Meneghini, R., Kozu, T., Kumagai, H., Boncyk, W.C., 1992. A study of rain estimation methods from space using dual-wavelength radar measurements at near-nadir incidence over ocean. J. Atmos. Ocean. Technol. 9, 364—382.

McLaughlin, D., Pepyne, D., Chandrasekar, V., et al., 2009. Short-wavelength technology and the potential for distributed networks of small radar systems. Bull. Am. Meteorol. Soc. 90, 1797—1818.

Meneghini, R., Jones, J.A., Iguchi, T., Okamoto, K., Kwiatkowski, J., 2004. A hybrid surface reference technique and its application to the TRMM precipitation radar. J. Atmos. Ocean. Technol. 21, 1645—1658.

Meneghini, R., Kim, H., Liao, L., Jones, J.A., Kwiatkowski, J.M., 2015. An initial assessment of the surface reference technique applied to data from the dual-frequency precipitation radar (DPR) on the GPM satellite. J. Atmos. Ocean. Technol. 32, 2281—2296.

Mitrescu, C., L'Ecuyer, T., Haynes, J., Miller, S., Turk, J., 2010. CloudSat precipitation profiling algorithm-model description. J. Appl. Meteorol. Climatol. 49, 991—1003.

Meyers, P., Ferraro, R., Wang, N.-Y., 2015. Updated screening procedures for GPROF2010 over land: utilization for AMSR-E. J. Atmos. Ocean. Technol. 32, 1015—1028.

Mugnai, A., Smith, E.A., 1984. Passive microwave radiation transfer in an evolving cloud medium. In: IRS '84: Current Problems in Atmospheric Radiation. A. Deepak Publishing, Hampton, VA.

NOAA National Centers for Environmental Information (NCEI), 2024. U.S. Billion-Dollar Weather and Climate Disasters. https://doi.org/10.25921/stkw-7w73. https://www.ncei.noaa.gov/access/billions/.

Oakley, N.S., Liu, T., McGuire, L.A., Simpson, M., Hatchett, B.J., Tardy, A., Kean, J.W., Castellano, C., Laber, J.L., Steinhoff, D., 2023. Toward probabilistic post-fire debris-flow hazard decision support. Bull. Am. Meteorol. Soc. 104, E1587—E1605.

Olson, W.S., 1989. Physical retrieval of rainfall rates over the ocean by multispectral microwave radiometry: application to tropical cyclones. J. Geophys. Res. 94, 2267—2280.

Palmer, W., 1965. Meteorological Drought. U.S. Research Paper No. 45. U.S. Weather Bureau, Washington, DC.

Peral, E., Im, E., Wye, L., Lee, S., Tanelli, S., Rahmat-Samii, Y., Horst, S., Hoffman, J., Yun, S.H., Imken, T., Hawkins, D., 2018. Radar technologies for earth remote sensing from CubeSat platforms. Proc. of the IEEE. 106 (3), 404—418.

Perica, S., Pavlovic, S., Laurent, M.S., Trypaluk, C., Unruh, D., Martin, D., Wilhite, O., 2015. Precipitation- frequency Atlas of the United States (volume 10, version 3.0), NOAA Atlas 14. In: National Oceanic and Atmospheric Administration. Silver Spring, Maryland.

Petty, G.W., 2006. A First Course in Atmospheric Radiation. Sundog Publishing, Madison, WI, p. 459.

Pfreundschuh, S., Guilloteau, C., Brown, P.J., Kummerow, C.D., Eriksson, P., 2024. GPROF V7 and beyond: assessment of current and potential future versions of the GPROF passive microwave precipitation retrievals against ground radar measurements over the continental US and the Pacific Ocean. Atmos. Meas. Tech. 17, 515—538.

Ringerud, S., Kummerow, C., Peters-Lidard, C., Tian, Y., Harrison, K., 2015. A semi-empirical model for computing land surface emissivity in the microwave region. IEEE Trans. Geosci. Rem. Sens. 53, 1935—1946.

Rosenfeld, D., Gutman, G., 1994. Retrieving microphysical properties near the tops of potential rain clouds by multispectral analysis of AVHRR data. Atmos. Res. 34, 259—283.

Rossi, G., Catani, F., Leoni, L., Segoni, S., Tofani, V., 2013. HIRESSS: a physically based slope stability simulator for HPC applications. Nat. Hazards Earth Syst. Sci. 13, 151—166.

Sadeghi, M., Nguyen, P., Naeini, M.R., et al., 2021. PERSIANN-CCS-CDR, a 3-hourly 0.04° global precipitation climate data record for heavy precipitation studies. Sci. Data 8, 157.

Sapiano, M.R.P., Smith, T.M., Arkin, P.A., 2008. A new merged analysis of precipitation utilizing satellite and reanalysis data. J. Geophys. Res. 113, D22103. https://doi.org/10.1029/2008JD010310.

Schmit, T.J., Griffith, P., Gunshor, M.M., Daniels, J.M., Goodman, S.J., Lebair, W.J., 2017. A closer look at the ABI on the GOES-R series. Bull. Am. Meteorol. Soc. 98, 681—698.

Scofield, R.A., 1987. The NESDIS operational convective precipitation technique. Mon. Weather Rev. 115, 1773—1792.

Scofield, R.A., Kuligowski, R.J., 2003. Status and outlook of operational satellite precipitation algorithms for extreme-precipitation events. Weather Forecast. 18, 1037—1051.

Seliga, T.A., Bringi, V.N., 1976. Potential use of radar differential reflectivity measurements at orthogonal polarizations for measuring precipitation. J. Appl. Meteorol. Climatol. 15, 69—76.

Seto, S., Takahashi, N., Iguchi, T., 2005. Rain/no-rain classification methods for microwave radiometer observations over land using statistical information for brightness temperatures under no-rain conditions. J. Appl. Meteorol. 44, 1243—1259.

Skamarock, W.C., Klemp, J.B., Dudhia, J., Gill, D.O., Barker, D., Duda, M.G., Powers, J.G., et al., 2008. A Description of the Advanced Research WRF Version 3. University Corporation for Atmospheric Research. No. NCAR/TN-475+STR. https://doi.org/10.5065/D68S4MVH.

Skofronick-Jackson, G., et al., 2017. The global precipitation measurement (GPM) mission for science and society. Bull. Am. Meteorol. Soc. 98, 1679—1695.

Skofronick-Jackson, G., Kirschbaum, D., Petersen, W., et al., 2018. The Global Precipitation Measurement (GPM) mission's scientific achievements and societal contributions: reviewing four years of advanced rain and snow observations. Q. J. R. Meteorol. Soc. 144 (Suppl. 1), 27—48.

Smith, E.A., Lamm, J.E., Adler, R., Alishouse, J., Aonashi, K., Barrett, E., Bauer, P., Berg, W., Chang, A., Ferraro, R., Ferriday, J., Goodman, S., Grody, N., Kidd, C., Kniveton, D., Kummerow, C., Liu, G., Marzano, F., Mugnai, A., Olson, W., Petty, G., Shibata, A., Spencer, R., Wentz, F., Wilhert, T., Zipser, E., 1998. Results of WetNet PIP-2 project. J. Atmos. Sci. 55, 148—1536.

Smith, E.A., Xiang, X., Mugnai, A., Tripoli, G.J., 1994. Design of an inversion-based precipitation profile retrieval algorithm using an explicit cloud model for initial guess microphysics. Meteorol. Atmos. Phys. 54, 53—78.

Smith, G., 2003. Flash flood potential: determining the hydrologic response of FFMP basins to heavy rain by analyzing their physiographic characteristic Report to the NWS Colorado Basin River forecast center, 11 pp. Available online at: http://www.cbrfc.noaa.gov/papers/ffp_Wpap.pdf.

Spencer, R.W., Martin, D.W., Hinton, B., Weinman, J.A., 1983. Satellite microwave radiances correlated with radar rain rates over land. Nature 304, 141—143.

Spencer, R.W., Goodman, H.M., Hood, R.E., 1989. Precipitation retrieval over land and ocean with the SSM/I: identification and characteristics of the scattering signal. J. Atmos. Ocean. Technol. 6, 254—273.

Stephens, G., et al., 2002. The CloudSat mission and the ATrain. Bull. Am. Meteorol. Soc. 83, 1771—1790.

Sy, O.O., et al., 2022. Scientific products from the first radar in a CubeSat (RainCube): deconvolution, cross-validation, and retrievals. IEEE Trans. Geosci. Rem. Sens. 60, 1—20, 1000320.

Takahashi, N., Iguchi, T., 2008. Characteristics of TRMM/PR system noise and their application to the rain detection algorithm. IEEE Trans. Geosci. Rem. Sens. 46, 1697—1704.

Todd, M.C., Barrett, E.C., Beaumont, M.J., Green, J.L., 1995. Satellite identification of rain days over the upper Nile river basin using an optimum infrared rain/no-rain threshold temperature model. J. Appl. Meteorol. 34, 2600—2611.

Todd, M.C., Barrett, E.C., Beaumont, M.J., Bellerby, T.J., 1999. Estimation of daily rainfall over the upper Nile river basin using a continuously calibrated satellite infrared technique. Meteorol. Appl. 6, 201—210.

Toyoshima, K., Masunaga, H., Furuzawa, F., 2015. Early evaluation of Ku- and Ka-band sensitivities for the global precipitation measurement (GPM) dual-frequency precipitation radar (DPR). SOLA 11, 14—17.

Tourville, N., Stephens, G., DeMaria, M., Vane, D., 2015. Remote sensing of tropical cyclones. Bull. Am. Meterol. Soc. 96, 609—622.

Turk, F.J., Miller, S.D., 2005. Toward improved characterization of remotely sensed precipitation regimes with MODIS/AMSR-E blended data techniques. IEEE Trans. Geosci. Rem. Sens. 43, 1059—1069.

Vicente, G.A., Scofield, R.A., Menzel, W.P., 1998. The operational GOES infrared rainfall estimation technique. Bull. Am. Meterol. Soc. 79, 1883—1898.

Vicente, G.A., Davenport, J.C., Scofield, R.A., 2002. The role of orographic and parallax correction on real-time high resolution satellite rainfall rate distribution. Int. J. Rem. Sens. 23, 221—230.

Vila, D.A., Machado, L., Laurent, H., Velasco, I., 2008. Forecast and tracking of cloud cluster (ForTraCC) using satellite infrared imagery: methodology and validation. Weather Forecast. 23, 233—245.

Walther, A., Heidinger, A., 2012. Implementation of daytime cloud optical and microphysical properties algorithm (DCOMP) in PATMOS-x. J. Appl. Meteorol. Climatol. 51, 1371—1390.

Wang, J.-J., Adler, R.F., Huffman, G.J., Bolvin, D., 2014. An updated TRMM composite climatology of tropical rainfall and its validation. J. Clim. 27 (1), 273—284.

Waterman, P.C., 1965. Matrix formulation of electromagnetic scattering. In: Proc. IEEE, 53, pp. 805—812.

Wehr, T., Kubota, T., Tzeremes, G., Wallace, K., Nakatsuka, H., Ohno, Y., Koopman, R., Rusli, S., Kikuchi, M., Eisinger, M., Tanaka, T., Taga, M., Deghaye, P., Tomita, E., Bernaerts, D., 2023. The EarthCARE mission — science and system overview. Atmos. Meas. Tech. 16, 3581—3608.

Weng, F., Grody, N.C., 1994. Retrieval of cloud liquid water using the special sensor microwave imager (SSM/I) data. J. Geophys. Res. 99, 25535—25551.

Weng, F., Zhao, L., Poe, G., Ferraro, R., Li, X., Grody, N., 2003. AMSU cloud and precipitation algorithms. Radio Sci. 338, 8068—8079.

Wentz, F.J., Draper, D., 2016. On-orbit absolute calibration of the global precipitation measurement microwave imager. J. Atmos. Ocean. Technol. 33, 1393—1412.

Weinman, J., Guetter, A., 1977. Determination of rainfall distributions from microwave radiation measured by the Nimbus 6 ESMR. J. Appl. Meteorol. 16, 437—442.

Wilheit, T.T., Chang, A., Rao, M., Rodgers, E., Theon, J., 1977. A satellite technique for quantitatively mapping rainfall rates over the oceans. J. Appl. Meteorol. 16, 551—560.

Wilheit, T.T., Kummerow, C., Ferraro, R., 2003. Rainfall algorithms for AMSR-E. IEEE Trans. Geosci. Rem. Sens. 41, 204—214.

Wilhite, D.A. (Ed.), 2005. Drought and Water Crises: Science, Technology, and Management Issues, first ed. CRC Press. https://doi.org/10.1201/9781420028386.

Williams, C.R., et al., 2014. Describing the shape of raindrop size distributions using uncorrelated raindrop mass spectrum parameters. J. Appl. Meteorol. Climatol. 53, 1282—1296.

Woodley, W.L., Sancho, R., 1971. A first step towards rainfall estimation from satellite cloud photographs. Weather 26, 279—289.

Wright, D.B., Smith, J.A., Villarini, G., Baeck, M.L., 2013. Estimating the frequency of extreme rainfall using weather radar and stochastic storm transposition. J. Hydrol. 488, 150—165. https://doi.org/10.1016/j.jhydrol.2013.03.003.

Wright, D.B., Yu, G., England, J.F., 2020. Six decades of rainfall and flood frequency analysis using stochastic storm transposition: review, progress, and prospects. J. Hydrol. 585, 124816. https://doi.org/10.1016/j.jhydrol.2020.124816.

Wu, H., Adler, R.F., Tian, Y.D., Huffman, G.J., Li, H.Y., Wang, J.J., 2014. Real-time global flood estimation using satellite-based precipitation and a coupled land surface and routing model. Water Resour. Res. 50, 2693—2717.

Xie, P., Joyce, R., Wu, S., Yoo, S., Yarosh, Y., Sun, F., Lin, R., 2017. Reprocessed, bias-corrected CMORPH global high-resolution precipitation estimates from 1998. J. Hydrometeorol. 18, 1617—1641.

Xie, P., Sinsky, E., Wu, S., DeWitt, D., Garrett, D., Wang, W., 2023. Operational real-time production of CMORPH2. In: EGU General Assembly 2023, Vienna, Austria, 24—28 Apr 2023, EGU23-2792. https://doi.org/10.5194/egusphere-egu23-2792.

Xu, W., Adler, R., Wang, N.-Y., 2013a. Improving geostationary satellite rainfall estimates using lightning observations: underlying lightning-rainfall-cloud relationships. J. Appl. Meteorol. 52, 213—229.

Xu, W., Adler, R., Wang, N.-Y., 2013b. Combining satellite infrared and lightning information to estimate warm season convective and stratiform rain. J. Appl. Meteorol. Climatol. 53, 180—199.

Yang, Y., Tang, G., Lei, X., Hong, Y., Yang, N., 2018. Can satellite precipitation products estimate probable maximum precipitation: a comparative investigation with gauge data in the dadu River Basin. Rem. Sens. 10, 41. https://doi.org/10.3390/rs10010041.

Zhang, J., et al., 2016a. Multi-radar multi-sensor (MRMS) quantitative precipitation estimation: initial operating capabilities. Bull. Am. Meteorol. Soc. 97, 621—638.

Zhang, K., et al., 2016b. iCRESTRIGRS: a coupled modeling system for cascading flood-landslide disaster forecasting. Hydrol. Earth Syst. Sci. 20, 5035—5048.

Zhao, K., Huang, H., Lu, Y., Chen, H., et al., 2024. Operational phased array radar network for natural hazard monitoring and warnings in urban environments over the greater Bay area, China. Bull. Am. Meteorol. Soc. in press.

Zhao, L., Weng, F., 2002. Retrieval of ice cloud parameters using the AMSU. J. Appl. Meteorol. 41, 384—395.